HEPATOCELLULAR ADENOMA CLASSIFICATION USING MRI AND IDENTIFICATION OF BIOMARKERS FOR PREDICTION OF LIVER TUMOR ONSET IN A MOUSE MODEL OF GLYCOGEN STORAGE DISEASE TYPE1a.

R.Resaz

INDEX

1. INTRODUCTION

1.1 Hepatocellular adenoma

Hepatocellular adenomas (HCA) are benign tumors caused by proliferation of hepatocytes with a high content of glycogen and fat. They constitute 2% of all liver tumors and their most important complications are hemorrhage and malignant transformation to hepatocellular carcinoma (HCC) (1).

HCA are characterized by a tumor parenchyma with numerous arteries, unaccompanied by bile ducts and a cytoplasm that may be either normal, glycogenotic or steatotic. They show sinusoidal dilatation, infarcts, and haemorrhage, and may result in oedematous or fibrotic regions. Haemorrhage is more frequent in HCA with sinusoidal dilatation and congestion (2), and can usually occur in HCA bigger than 4–5 cm. Haemorrage can be either inside the nodule, usually admixed with necrotic changes, or spontaneous haemorrhagic rupture which can cause subcapsular haematoma and haemoperitoneum. The diagnosis of HCA is usually made on routine HE staining, while immunohistochemistry is necessary for the classification into the different subtypes (3), that is important for the follow-up and management of the patient (4). In fact, HCA are monoclonal tumors characterized by several recurrent mutations (5-8) and are subclassified into 4 groups, according to their genotype and phenotype (5).

- HHCA, characterized by inactvating mutation of *HNF1A* gene.

HNF1A gene encodes the Hepatocyte Nuclear Factor 1 α (HNF1α). a tumor suppressor gene involved in liver tumorigenesis (6).

HHCA account for the 35–40% of HCA and mostly correspond to a histologically homogeneous group of tumors, characterized by marked steatosis, no cytological abnormalities, no inflammatory infiltrates. Furthermore, *FABP1* (liver fatty acid binding protein), which is a gene positively regulated by *HNF1A*, and expressed in normal liver tissue, displays downregulated expression levels in HHCA. In fact, in immunohistochemistry, LFABP (liver fatty acid binding protein) is negative in the tumor while it shows a normal expression in the surrounding non-tumoral tissue (3). Tumor borders are well delineated because of the

differences in LFABP expression and presence of steatosis between tumor and adjacent normal liver. HHCA often show adenomatosis, as multiple adenomas of varying size, associated with a several steatotic micronodules.

- bHCA, characterized by activating mutations of the β-Catenin gene:

β-Catenin mutations activate the Wnt/β-catenin pathway that is involved in lineage specification, differentiation, stem cell renewal, proliferation, cell adhesion and liver regeneration. bHCA are at greater risk of malignant transformation, and mutations of β-catenin are also found in 20–30% of hepatocellular carcinomas. bHCA account for the 10–15% of HCA, and the usual anti-βcatenin immunohistochemical pattern results in an aberrant nuclear and cytoplasmic posititvity, distributed in a random and heterogenous pattern. Furthermore, *Glul*, a β-catenin target gene, coding for glutamine synthetase, also displays upregulated expression. Therefore, these bHCA show also strong and diffuse glutamine synthetase staining (3).

bHCA are often extremely difficult to distinguish from well-differentiated HCC, due to the cytological and architectural abnormalities. Moreover, they are also more frequently associated with the malignant transformation to HCC than other HCA subtypes (2-5). This subgroup of bHCA is overrepresented in male patients and specific risk factors are often found, such as male hormone administration, glycogenosis, and familial polyposis. However, death due to HCC was more often linked to women with this type of β-HCA in our own series (4).

- IHCA Inflammatory Hepatocellular Adenomas:

IHCA account for more than 50% of all HCA, and are characterized by the presence of inflammatory infiltrates, sinusoidal dilatation, thick-walled arteries, and ductular reaction. They show overexpression of molecules of the acute-phase inflammatory response, such as serum amyloid A (SAA) and C-reactive protein (CRP) (3), confirmed by immunohistochemical analysis.

Steatosis may be present and is usually distributed irregularly within the IHCA. Approximately 10% of IHCA have a mutation in the β-catenin gene.

The risk of HCC does also exist in these inflammatory/β-HCA, but in a proportion that is presently unknown.

Some HCA are associated with gain-of-function mutations caused by in-frame somatic deletions in the *IL6ST* gene (8). This gene encodes for the signalling co-receptor gp130. Mutant gp130 constitutively activates STAT3 signalling in the absence of IL-6 binding. *gp130 and* β-catenin mutations may coexist in a same HCA.

- UHCA, unclassified hepatocellular adenomas

Tumors in this group represent less than 5–10% of cases, and they do not show *HNF1A* or β-catenin gene mutations and do not express inflammatory proteins.

1.2 HCC

There is a small but definite incidence of malignant transformation of HCA (2-5). This could be demonstrated by the co-existence of both HCA and HCC within the same tumor and the occurrence of an overt HCC several years after partial resection of a HCA. However, the exact pathways of malignant transformation and the exact point at which the switch to malignant transformation occurs remain unknown. The risk of malignancy is particularly higher for bHCA, which are most frequently associated with glycogenosis type 1, androgenic hormone intake, and familial adenomatous polyposis. Since bHCA often show cytological atypia and pseudoglandular pattern, it is often very difficult and sometimes almost impossible to differentiate these from a well-differentiated HCC. Although glypican-3 is a promising marker for the identification of HCC, its utility is limited by the fact that it may not be detected in approximately one third of HCC which develop in a normal liver. In inflammatory HCA, we suspect that β-catenin mutation is a secondary event that occurs at a late time.

HCA occurs in women with a history of oral contraception and in other conditions such as Fanconi's anemia and metabolic syndrome [9]. It has been reported that malignancy within HCA in women with a history of oral contraception is rather

low (< 4%), while the risk of malignant transformation in men is 10 times more frequent and is mostly associated with metabolic syndrome (10). HCA is also often are associated with Glycogen Storage Disease (GSD), especially type I and III.

1.3 Glycogen Storage Disease

GSD1a is an autosomal recessive metabolic disorder that occurs approximately once in every 100,000 live births (11). GSD1a is caused by a mutation in the catalytic subunit of glucose-6-phosphatase-α (G6Pase–α) (12), a key enzyme in glucose homeostasis. G6Pase-α is expressed primarily in liver, kidney and intestine, and catalyzes the hydrolysis of glucose-6-phosphate (G6P) to glucose and phosphate (13), the terminal steps in gluconeogenesis and glycogenolysis (Fig. 1).

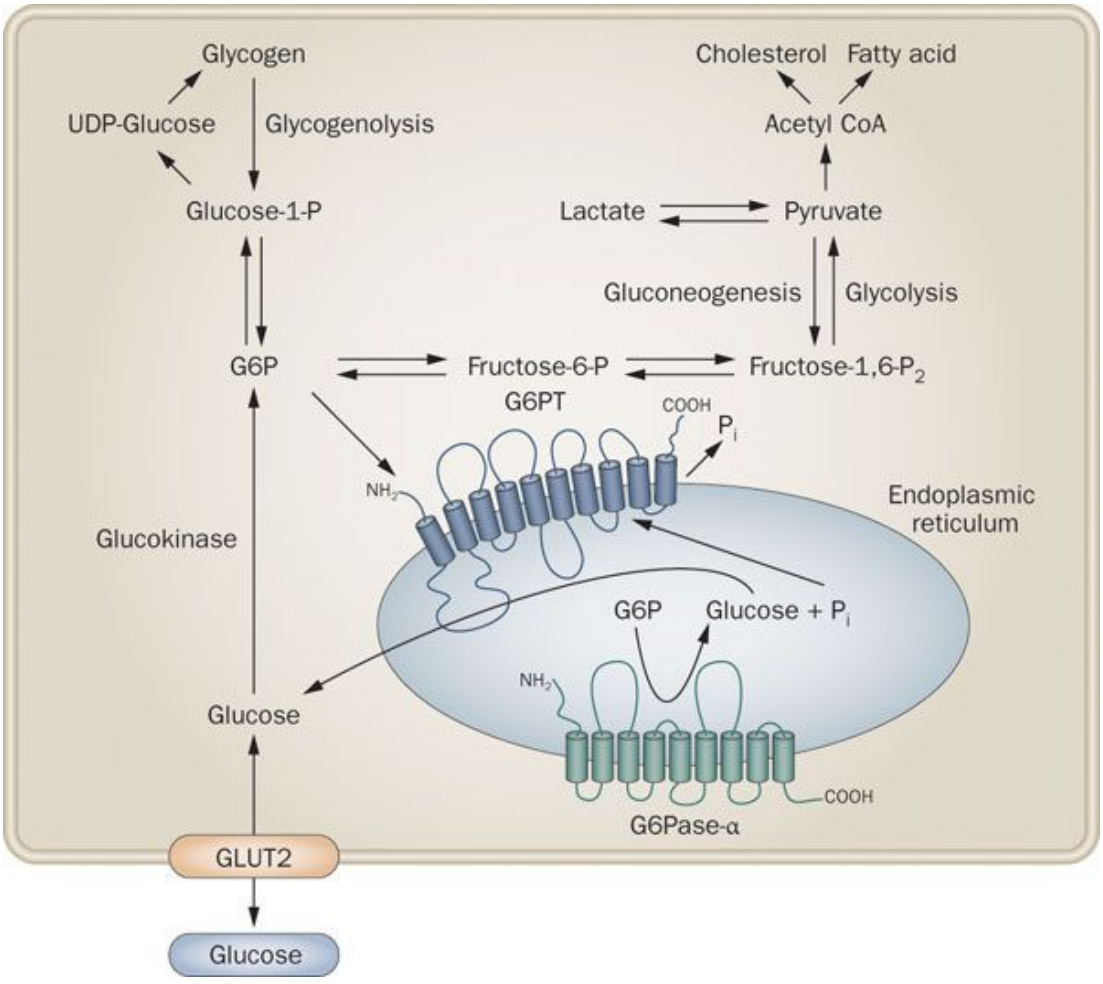

From Chou JY, The Molecular Basis of Type 1 Glycogen Storage Diseases, 2001

Figure 1. The primary anabolic and catabolic pathways of G6Pase in gluconeogenic organs. G6Pase-α is shown embedded within the membrane of the endoplasmic reticulum. GLUT2, the transporter responsible for the transport of glucose in and out of the cell in liver, kidney and intestine, is shown embedded in the plasma membrane. Abbreviations: G6P, glucose-6-phosphate; G6Pase-α, glucose-6-phosphatase-α; G6PT, glucose-6-phosphate transporter; GLUT2, glucose transporter 2, P, phosphate; P' inorganic phosphate; UDP uridine diphosphate.

GSD1a patients are unable to maintain glucose homeostasis and show growth retardation, hypoglycemia, hepatomegaly, kidney enlargement, hyperlipidemia, hyperuricemia, and lactic acidemia. Long-term symptoms include gout, osteoporosis, renal failure, and hepatic adenomas with risk for malignancy. The disease is controlled by dietary therapies, which consist of continuous nasogastric infusion of glucose (14) or frequent oral administration of uncooked cornstarch (15), to prevent hypoglycemia.

Unfortunately, the control of hypoglycemia cannot prevent the progressive deterioration of liver and kidney. Liver dysmetabolism is severe, hepatocytes become enlarged and loaded with glycogen and triglycerides containing vesicles, and the hematochemical parameters are altered with high triglycerides and cholesterol content. Persistency of liver dysmetabolism during patient's ageing results in a progressive worsening of the clinical parameters, like the formation of hepatocellular adenomas (HCA), which are likely to be multifocal, and progress to liver carcinoma (HCC) in 10% of the cases (16-18). 52% of GSD adenomas can be classified as IHCA, 28% as bHCA, and the remaining 20% as UHCA (19). The elevated percentage of adenomas with β-catenin activating mutations may explain the risk of malignant transformation of HCA in HCC in GSD1a patients.

Liver transplant is the only option in the most severe cases. GSD1a patients exhibit marked variability in the severity of symptoms and complications and the underlying pathological pathways that develop with the progress of the disease are poorly understood. The underlying pathological pathways that develop with age are poorly understood, and there are no biomarkers associated with the variability of the progressive tissue alterations (20), no indication of causes of the

worsening of the clinical situation and no treatment protocol to deal with the HCA/HCC.

1.4 Animal Models

There are two main mouse models for GSD-1a, closely mimicking the human disorders. The first model, developed by Dr. Chou is a KO mouse ($G6pc^{-/-}$) (21). These animals are very fragile, they die within three weeks after birth, if untreated, and, therefore, they are unsuitable for studying long-term complications of GSD1a. So, to provide insights into the progressive age-dependent liver degeneration in GSD-1a, we have developed in 2014 a new and clinically relevant murine model, LS-$G6pc^{-/-}$, conditional for the liver, that displays variability in the severity of the complications and the long-term consequences of the hepatic degeneration, similar to what is observed in GSD-1a patients (22).

1.5 LS-*G6pc*$^{-/-}$ mice

LS-$G6pc^{-/-}$ mice manifest a milder pathological situation in comparison with $G6pc^{-/-}$ mice. Nevertheless, LS-$G6pc^{-/-}$ mice exhibit hepatic symptoms similar to those of the human GSD-1a and, therefore, represent a valid model to evaluate long-term complication and HCA progression (22).

Histology and histochemistry

LS-$G6pc^{-/-}$ mice are viable and fertile and show no growth retardation. On the other hand, LS-$G6pc^{-/-}$ mice manifest a liver phenotype typical of GSD-1a, characterized by hepatomegaly. This clinical presentation in GSD-1a is primarily caused by excess of glycogen and lipid deposition. LS-$G6pc^{-/-}$ mic show marked glycogen deposit in the hepatocytes, compared with WT mice (Fig. 2A, B). Steatosis in LS-$G6pc^{-/-}$ mice is revealed by the presence of macro- and micro-lipid vesicles in the enlarged hepatocytes (Fig. 2A, arrows). Activity of G6Pase is detectable in the livers of wild type mice (Fig. 2D), in contrast to the livers of LS-$G6pc^{-/-}$ mice for which staining is negative (Fig. 2C).

The glycogen content in the livers of LS-$G6pc^{-/-}$ mice is significantly higher than that of control, increasing with mice ageing to reach 60mg/g of liver in 10-15

month old mice (Fig. 2E, F). Similarly, accumulation of triglycerides in LS-G6pc$^{-/-}$ livers significantly increases with age, in agreement with the marked Oil red O staining of liver sections (Fig. 2G, H) (22).

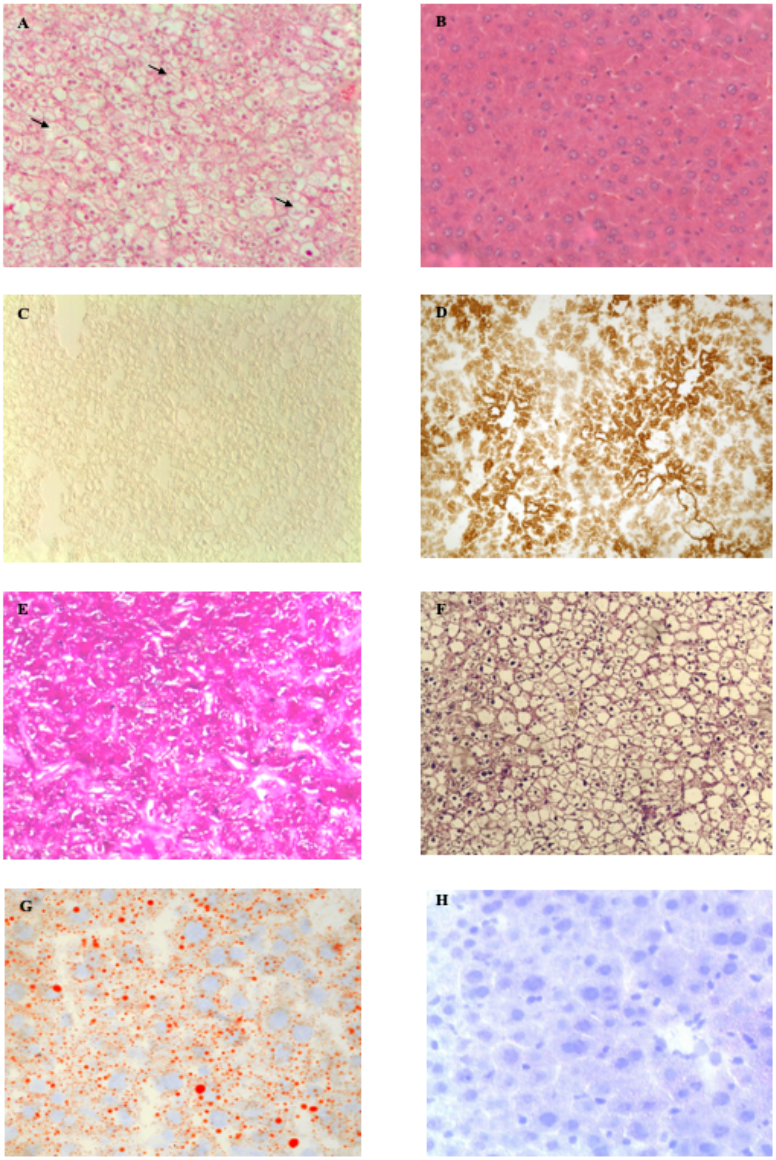

Figure 2. Histological and histochemical analysis of livers from LS-G6pc$^{-/-}$ and control mice. Paraffin-embedded, H&E-stained liver sections from a 2 month old LS-G6pc$^{-/-}$ mouse (A) and control mouse (B). To evaluate the G6Pase activity, liver cryostat sections were treated as described in Material and Methods. Colored lead sulfide was developed with ammonium sulfide. Representative results of liver sections from 3 month old LS-G6pc$^{-/-}$ (C) and control (D) mice are shown. Paraffin-embedded liver sections from a 3 month old LS-G6pc$^{-/-}$ mice were stained with PAS (E) or PAS plus diastase (F). Oil red O staining of LS-

G6pc$^{-/-}$ mouse (A) or control mouse (B) liver cryostat sections at 2 months of age shows lipid accumulation in the hepatocytes of LS-G6pc$^{-/-}$ mouse. (A, B, E and F) 10X magnification, (C, D, G and H) 20X magnification.

Metabolic characteristics of LS-G6pc$^{-/-}$ mice.

Glu-6- P phosphohydrolase activity in the liver of LS-G6pc$^{-/-}$ is undetectable (Fig. 3A).

LS-G6pc$^{-/-}$ mice suffer from fasting hypoglycemia typical of GSD-1a. The mean serum glucose level in LS-G6pc$^{-/-}$ mice is significantly lower than that in control littermates after 6 hours fasting (Fig. 3B). These mice, though, do not suffer from hypoglycemic seizure and therefore do not require glucose therapy, like the G6pc$^{-/-}$ mice (21). In fact, in the fed state, the mean blood glucose concentration in LS-G6pc$^{-/-}$ mice is 25% lower than in control mice, but remained within the normal levels. Moreover, serum cholesterol and triglycerides mean levels are higher in LS-G6pc$^{-/-}$ mice 2-4 months old than in control littermates (Fig. 3C,D), but they show improvement of serum cholesterol and triglycerides levels in mice older that 6 months (Fig. 3C,D) (22).

Finally, alanine aminotransferase (ALT) and aspartate aminotransferase (AST) are moderately to mildly increased in LS-G6pc$^{-/-}$ mice as compared to healthy controls (data not shown).

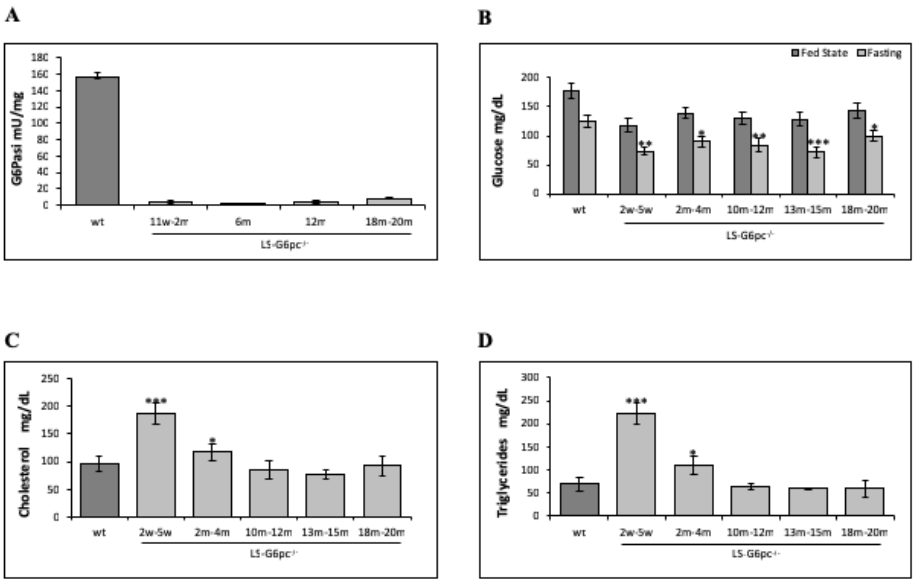

Figure 3. Hepatic G6Pase activity, plasma glucose, cholesterol and triglyceride levels in LS-G6pc$^{-/-}$ mice. Metabolic functions were analyzed in LS-G6pc$^{-/-}$ mice. 3 to 5 mice were analyzed for each group. G6Pase activity (A), blood glucose (B), triglycerides (C), and total cholesterol (D) were analyzed at the indicated ages in weeks (w) or months (m). Because of the similarities of the respective metabolites in each group of control mice, results shown are pooled data of age 2 weeks-20 months. 4 control mice were analyzed for each group. (A') Western blot analysis of liver tissues for G6Pase-α expression. (B) Glucose levels was determined in the fed state (dark grey bars) or upon 6 hrs fasting (light grey bars). Data are presented as mean ± SD. Values which are significantly different from control mice (P <0.05*, P <0.01** and ***$P < 0.005$) are indicated.

Progressive liver damage with age.

The severity of liver damage increases as mice grew older. By two months of age areas of paucicellular necrosis with inflammatory cells start to appear (Fig. 4A,B), and initial damage of liver structure could be observed by sinusoid and vein enlargement (Fig. 4C) (22).

In livers of older mice (aged 6 to 20 months) portal and periportal inflammatory infiltrates are detected (Fig. 4D). Moreover, marked amyloid deposition is observed in 90% of the livers of mice older than 10 months of age (Fig. 4E,F). Deposits is observed both in vessel walls and within sinusoids. The material is positive to Congo Red (Fig. 4F) and displays green birefringence when viewed under polarized light (data not shown), confirming amyloid deposition.

Thus, even if the metabolic parameters tend to normalize as the mice age, hepatic degeneration worsens and the progressive degeneration of the liver leads to premalignant and malignant transformation. By 10 months of age, 40% of LS-G6pc$^{-/-}$ mice develop HCA and HCC (Fig. 5A,B). Therefore, LS-G6pc$^{-/-}$ mice manifest most of the liver damages of GSD1a and develop hepatic long term-complications such as those affecting GSD1a patients (22).

Finally, LS-G6pc$^{-/-}$ mice develop marked vascular and sinusoidal amyloidosis. To our knowledge, amyloidosis has been reported only once in GSD1b patients (23) and never in GSD-1a patients or in the other GSD-1a animal models. However, the presence of amyloidosis in the livers of LS-G6pc$^{-/-}$ mice remains and further studies will be necessary to determine the reasons for the occurrence of this pathology.

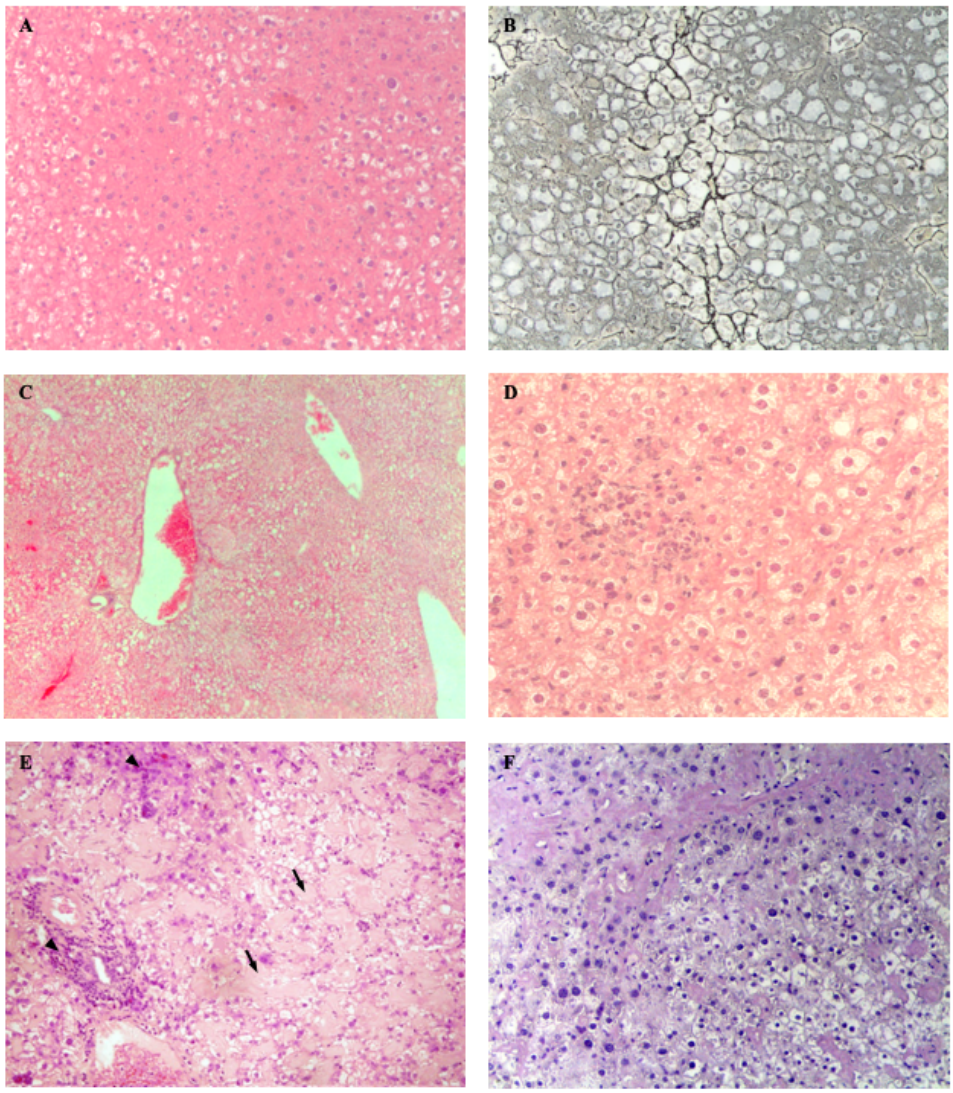

Figure 4. Histological appearance of liver in adult mouse. (A) H&E and (B) reticulin staining shows foci of necrosis in a 2 month old LS-G6pc$^{-/-}$ mouse. (C) Liver section of a 4 month old LS-G6pc$^{-/-}$ mouse showing sinusoid and vein enlargement. (D) Liver section of a 8 month old LS-G6pc$^{-/-}$ mouse with inflammatory infiltrates. (E) Liver section of a 15 month old LS-G6pc$^{-/-}$ mouse with inflammatory infiltrates (arrowheads) and sinusoidal amyloidosis (arrows) stained with H&E. (F) Extended amyloidosis is confirmed by Congo Red staining. (A, B, E and F) 10X magnification, (C) 4X magnification, (D) 20X magnification.

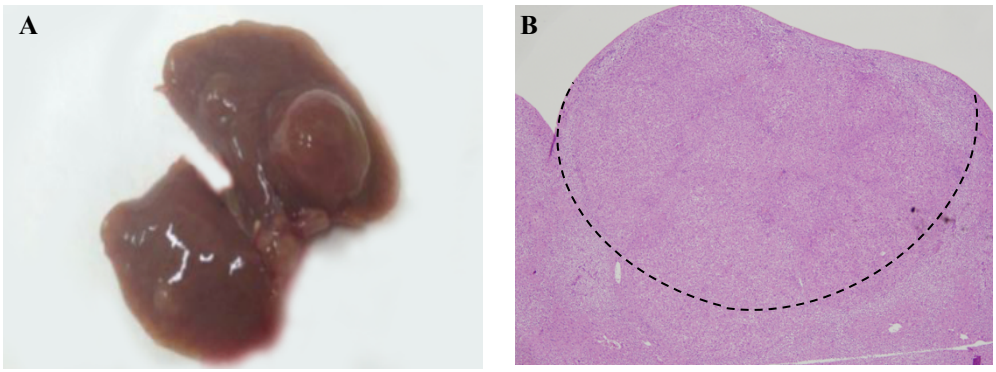

Figure 5. Liver nodules in ageing LS-G6pc$^{-/-}$ mice. (A) Liver resection of a 19 month old L-G6pc$^{-/-}$ mouse with a 10 mm nodule (arrow). Smaller nodules are also present (arrowhead). (B) H&E stained section from the liver of a 12 month old LS-G6pc$^{-/-}$ mouse showing a nodule histologically characterized as hepatocellular adenoma (boundry shown as dotted line).

2. AIM OF THE STUDY

The aim of this project has been to study liver degeneration and HCA and HCC development in the conditional mouse model of GSD1a, by using three different approaches:

2.1. MRI analysis of LS-*G6pc*$^{-/-}$ mice to identify and classify liver lesions.

Magnetic Resonance Imaging (MRI) represents an important tool to differentiate benign and malignant hepatic lesions especially because of the possibility to combine information obtained with different sequences, such as T1 and T2 weighted imaging (WI), diffusion WI (DWI) and post contrast T1WI using hepatobiliary gadolinium contrast agents, such as gadobenate dimeglumine (Gd-BOPTA) and gadoxetic acid (Gd-EOB) (24).

Correlation between MRI and the genotype-phenotype classification of HCA has been attempted (25-27). Characteristic MRI profiles for HHCA and IHCA have been identified while no specific MRI profile can be proposed for the identification of high-risk bHCA cases. In consideration of this, the subtyping and classification of liver adenomas for HCC risk prediction in humans still requires invasive procedures, i.e. biopsies.

A preclinical experimental approach may help to develop a method to better identify MRI features specifically associated with bHCA subtype. In this study we assessed the detection level and quantified the longitudinal evolution of liver lesions in LS-G6pc-/- mice in order to characterize HCA and HCC using a dedicated protocol, optimized for high magnetic field strength, and a hepato-specific contrast agent.

We show here that bHCA display MRI features distinguishable from those exhibited by IHCA or UHCA, indicating that MRI is a reliable method to identify high-risk HCA.

2.2 Proteomic analysis on liver specimens from LS-*G6pc*$^{-/-}$ mice.

Although transcriptional profiling provides an in-depth understanding of gene-expression changes in disease, limited agreement between transcriptional changes and protein level changes has been observed across various studies and in different cell types (28,29). Proteomic studies should provide an important perspective for

understanding pathophysiological changes that result in liver pathology (30). The simultaneous characterization of cell abundance of hundreds of proteins should make it possible to identify significant global protein expression changes in response to different biological conditions. To date, many studies have focused on characterizing diseased vs. normal liver proteomes (31,32). We determined the proteomic expression changes in the liver of LS-*G6pc*$^{-/-}$ mice in comparison with wild type mice to identify potential biomarkers of the pathophysiology of the affected liver. We show that LS-*G6pc*$^{-/-}$ livers display an age-dependent modulation of the expression of proteins belonging to specific biological processes associated with the progression of liver disease. Moreover, proteins that are hallmarks of hypoxia were persistently upregulated in the liver of these mice, while the acute inflammatory and immune response were among the significantly enriched biological processes in LS-*G6pc*$^{-/-}$ mice with adenomas in comparison with mice without tumors. Finally, different proteins involved in the process of tissue inflammation and macrophage polarization toward the M2 phenotype were upregulated. Our results are compatible with a metabolic reprogramming of glucose-6-P leading to enhanced glycolysis, lactate production, increased lipogenesis and cholesterol synthesis, and dysfunction in oxidative phosphorylation. Moreover, our results identify in the liver a pathologic environment, represented by hypoxia, inflammation, and macrophage M2 polarization, that may lead to tumor development and progression.

2.3 Identification of liver selective exosomal miRNA signatures on blood

The existence of a communication network between pathologic tissues and their environment through shedding of exosomes, membrane microvesicles transporting cellular contents, has been shown in several diseases including cancer (33-37). In vitro studies have revealed that exosomes can play an important role in the development and progression of cancer through modulation of intercellular communication within the tumor microenvironment by the transfer of protein, lipid, and RNA cargo. For example, breast cancer microvesicles stimulate angiogenesis and platelet-derived microvesicles promote tumor progression and metastasis of lung cancer cells (38,39). The exosomes have received a great deal of attention also for their biomarker potential. The utilization of blood exosomes

as surrogate tissue to diagnose, monitor, and predict disease evolution and response to therapy would be a poorly invasive, highly desirable alternative to biopsies. Furthermore, the use of exosomes seems to be an indispensable approach to deal with situations in which the pathological tissue is not readily available for analysis.

Exosomes may provide an excellent biomarker to monitor the emergence, progression, and prognosis of cancer, as well as the efficacy of treatment regimes. Studies have revealed that exosomes can be readily detected in many body fluids, and can be found in higher concentrations in the serum and plasma of cancer patients. The fact that exosomes often reflect the disease state and can be easily detected in bodily fluids makes them an ideal candidate for a non-invasive biomarker of tumor progression. Several reports identified potential exosomal biomarkers in patients' specimens (40). MicroRNA (miRNA) are exosome constituents actively studied as biomarkers for their stability, as diagnostic/prognostic indicators for their mirroring cellular components and as source of indication of therapeutic targets for their biological activities. miRNA are small cellular RNA inhibiting gene expression and often form a tissue selective pattern. Aberrant miRNA expression profiles were reported in cancer, rare diseases, and tissue degeneration (41). Therefore, the analysis of blood exosomes is a choice approach to study pediatric diseases because of the difficulties in obtaining tissue specimens. Our animal model, in which only the liver is affected, is ideal to identify exosomal miRNA contribution the specific pathologic manifestations of liver. This approach focuses on exosomal miRNA (exo-miR) evaluation in the blood of LS-G6pc$^{-/-}$ mice GSD1a patients to derive specific biomarkers and prognostic indicators of HCA onset and progression.

3. MATERIALS AND METHODS

3.1 Housing and breeding of mice

All animals were maintained in a conventional animal facility in 12-h light/dark cycles, fed at libitum, and monitored for their lifespan. All animal studies were reviewed and approved by the Ethical Committee for Animal Experimentation (CSEA) as Animal Use project n. 291 communicated to the Italian Ministry of Health having regard to the article of the D.lgs 116/92, and carried out at the animal facility of the National Institute for Cancer Research (Genova, Italy).

3.2. MRI analysis in mice

MRI was performed with a clinical 3T MR system (Signa EXCITE®HDxT, GE, Milwaukee, USA). Qualitative and quantitative analysis were performed on a commercially available workstation (AW Volume Share 2, ADW 4.4, GE, Milan, Italy).

Mice were anesthetized by intraperitoneal injection of xylazine (30 mg/kg) and ketamine (100 mg/kg) and positioned in a prototype coil, (birdcage linear coil, transmit/receive coil, 100 mm long, 55 mm of diameter, tuned at 127.6 MH, Flick Engineering Solutions BV&Baio G&GE Milwaukee, USA), placed on a support filled with warm water to preserve mice from hypothermia. For contrast enhancement 0,05 mmol/kg body weight gadobenate dimeglumine (MultiHance®) was administered by tail vein injection. The room temperature during experiments was 23°C, and the mean acquisition time was limited to 35 min, by the spontaneous awakening of mice.

Short localizer sequence was performed and the Field of View (FOV) was centered on the upper abdomen.

Based on these images, coronal before and after contrast administration T1-weighted and T2-weighted scans were planned and acquired with parameters and chronological order shown in Table 1. Each pre- and post-contrast sequence lasted about 7 minutes. The acquisition of all scans lasted about 25 minutes. To obtained a hepatobiliary contrast phase (HBP) the T1-WI sequences were acquired about 10 minutes after contrast administration.

Sequence type	Pre-contrast T1-WI-3D-FSPGR	T2-WI-FRFSE	Post-contrast T1-WI-3D-FSPGR
Acquisition Order	1	2	3
Plane	Coronal	Coronal	Coronal
TR (ms)	7.6	4700	7.6
TE (ms)	2.4	84.7	2.4
Bandwidth	50	31.2	50
FOV (mm)	10x7.5	10x6	10x7.5
Thickness (mm)	0.8	1	0.8
Acquisition Time (m:s)	07:10	07:36	07:10

Table 1. MRI imaging protocol parameters at 3 T scanner. The pre- and post-contrast sequence types are: T1-WI-3D-FSPGR, T1-WI Three Dimensional Fast Spoiled Gradient-echo 1 sequence; T2-WI-FRFSE, T2-WI-Fast Relaxation Fast Spin Echo 2 Sequence. The repetition time (TR) and the time of echo (TE) are determined by the user to control image contrast and the weighting of the MR image and are measured in milliseconds (ms). Bandwidth is a measurement parameter that represents the frequency spectrum (minimum to maximum processed frequency) of a pulse sequence acquired by a radio frequency system. The FOV (Field Of View) delineates the area to be imaged. Contrast injection lasted about 1:30 (minutes:seconds, m:s). Post contrast T1-WI acquisition started 9 minutes after contrast injection.

A total of 40 animals aged 13-18 months were scanned by MRI and checked for focal lesions in all sequences acquired. 25 mice were scanned once and sacrificed after the MRI session. The remaining 15 mice were monitored every four weeks for three months to evaluate lesion growth and complication onset such as rupture and bleeding (see Table 2).

Number of mice	Age of mice at first MRI (months)	Age of mice at last MRI (months)	Number of MRI analysis performed	Time of sacrifice
4	19	NA	1	Right after image acquisition
10	17 (7) e 18 (3)	NA	1	Right after image acquisition
9	15 (4) e 16 (5)	NA	1	Right after image acquisition
2	14	NA	1	Right after image acquisition
Total: 25				
4	13	16	3 (Every four weeks for 3 months)	Right after last MRI analysis
6	14	17	3 (Every four weeks for 3 months)	Right after last MRI analysis
5	15	18	3 (Every four weeks for 3 months)	Right after last MRI analysis
Total: 15				

Table 2. Study protocol. 25 mice aged 13-18 months were analyzed by MRI and sacrificed after image acquisition. 15 mice aged 13-15 months were analyzed by MRI every 4 weeks for 3 consecutive months and then sacrificed for further analysis.

We applied a qualitative analysis using a 5-point scale both to T1 and T2WI; the reader assessed the SI of the representative liver lesion relative to the adjacent liver parenchyma: 1 = very hypointense, 2 = mildly hypointense, 3 = isointense, 4 = mildly hyperintense, and 5 = very hyperintense (as biliary cysts) (42).

Lesions analyzed on the pre-contrast T1-WI and T2-WI were dimly identified compared with the liver parenchyma: all lesions were isointense on pre-contrast T1-WI and showed different signal on T2-WI (hyperintense or isointense, see below). Imaging acquired after contrast administration allowed to clearly detect hepatic lesions and to qualitatively distinguish 4 different patterns of contrast

uptake: isointense, very hyperintense, and very hypointense lesions, and lesions with a peripheral contrast enhancement (Fig. 6A-E).

These experiments demonstrated that the optimized parameters shown in Table 1 allow precise/high spatial resolution MR imaging of small size murine liver tumors. In fact, 18 of 40 animals (45%) showed development of focal lesions, ranging between 1 and 10 mm in diameter, with different combination of MRI characteristics and mainly detectable on contrast-enhanced T1-WI. We observed a total number of 41 liver lesion (Table 3 and Table 4).

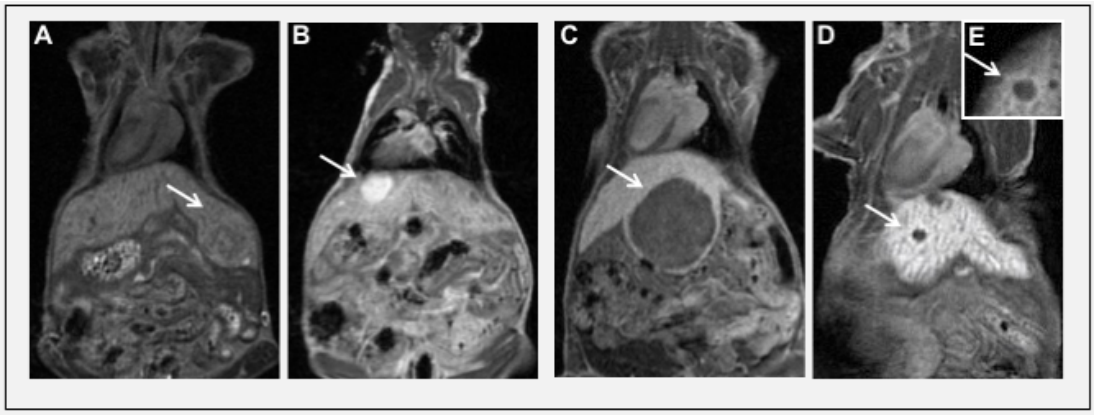

Figure 6. Different enhancement patterns of focal hepatic lesions. LS-G6pc$^{-/-}$ mice were scanned by MRI. The four different patterns of contrast uptake are shown. (**A**) Isointense. (**B**) Hyperintense. (**C**) Hypointense. (**D** and **E**) Hypointense lesions with peripheral rim of contrast enhancement from two different mice are shown. Lesions are indicated by arrows.

SUBTYPE		T1-WI BEFORE CONTRAST		T2-WI		T1-WI AFTER CONTRAST			
		Isointense	Hyperintense/ Hypointense	Isointense	Hyperintense	Isointense	Hyperintense	Hypointense with peripheral rim enhancement	Hypointense
IHCA[a]	SAA+/GS-	17/18	0/18	17/18	0/18	0/18	11/18	6/18	0/18
	SAA+ GS+	1/18	0/18	1/18	0/18	0/18	1/18	0/18	0/18
bHCA[b]	GS+ SAA-	8/8	0/8	0/8	8/8	0/8	0/8	0/8	8/8
HCC[c]	GS+	3/3	0/3	0/3	3/3	1/3	0/3	0/3	2/3
UHCA[d]	SAA-/GS-	12/12	0/12	12/12	0/12	2/12	1/12	2/12	7/12

1

Table 3. MRI characteristics of the lesions in G6pc-/- liver. Animals were scanned by MRI and checked for focal lesions. Nodules were characterized by immunohistochemistry.

[a]IHCA lesions were isointense on T1-WI before contrast administration and on T2-WI. On T1_WI, after contrast administration, 12/18 lesions were hyperintense and 6/18 lesions were hypointense with peripheral rim of contrast enhancement.

[b]bHCA were isointense on T1-WI before contrast administration, hyperintense on T2-WI, and hypointense on T1-WI after contrast administration.

[c]HCC were isointense on T1-WI before contrast enhancement and hyperintense on T2-WI. On T1- WI, after contrast administration, 2/3 HCC were hypointense and 1/3 was iso/hypointense.

[d]UHCA were isointense on T1-WI before contrast enhancement and on T2. After contrast administration on T1-WI, 2/12 lesions were isointense, 1/12 was hyperintense, 2/12 were hypointense with peripheral rim of contrast enhancement, and 7/12 were hypointense.

SAA: anti serum amyloid A2; GS: glutamine synthetase.

Mice with nodules	Total number of nodules	IHCA	bHCA	UHCA	HCC
1	1			1	
2	1			1	
3	4	3	1		
4	2			2	
5	1	1			
6	4	2	1		1
7	2	1		1	
8	2	1	1		
9	1				1
10	1			1	
11	3	1		2	
12	2	1		1	
13	3	2	1		
14	3	1	1		1
15	5	2*	1	2	
16	4	1	1	2	
17	1	1			
18	1		1		
Total number of nodules	41	18	8	12	3

Table 4. Number and type of lesions in LS-G6pc$^{-/-}$ mice. 18 mice showed presence of focal lesions by MRI analysis. Nodules were analyzed by immunohistochemistry. A total of 41 lesions were characterized. 18/41 tumors were classified as IHCA, 8/41 as bHCA, 12/41 as UHCA, and 3 were HCC.

*One lesion stained positive for SAA and negative for GS; one stained positive for both SAA and GS, and was therefore considered a high-risk HCA.

3.3 Histology and immunohistochemistry

Mice were sacrificed shortly after the last MRI acquisition.

All livers were macroscopically analyzed for focal hepatic nodules. Before liver sampling, the orientation of all liver lobes, relative to the longitudinal, transversal, and sagittal axis of the animal, was marked and the size and location of the macroscopic tumor nodes was measured with a caliper and correlated to the MRI findings. Part of the respective liver was then embedded in paraffin and used for diagnostic procedures. The rest of the liver was saved frozen for further analysis. All tissue samples were fixed in 10% buffered formalin for 24 hours and paraffin embedded. For histological analysis four micrometer thick serial sections were stained with hematoxylin and eosin. Reticulin was visualized by Gomori stain. Immunostaining was performed with anti-glutamine synthetase (GS; dilution 1:500, Abcam, Cambridge, UK) and anti-serum amyloid A (SAA; dilution 1:100, Cloud-Clone Corp., Houston, TX, USA) antibodies. Reactions were developed using DAKO EnVision+ System-HRP (DAB) (DAKO North America Inc. Carpinteria, California, USA). After immunostaining slides were counterstained with haematoxylin. Positive and negative controls were included for each run.

3.4 Sample collection, histology, and phenotype analyses

Mice were grouped according to their age into 6 groups, from 1 month to 18 months, three months apart. Mice were anesthetized and blood was drawn from the left ventricle with a syringe. Livers were sectioned, partly frozen for proteomic analysis and partly fixed in 10% buffered formalin for 24 hours. Formalin fixed tissue was then processed and from paraffin embedded tissue, four micrometer thick sections were cut and stained with haematoxylin and eosin for histological analysis. All animals were phenotypically evaluated as described (22).

Mice were histologically evaluated for liver lesions. Mice showed different degree of glycogen and lipid accumulation, and six out of twenty LS-G6pc$^{-/-}$ mice developed at least one hepatic adenoma. Livers of WT mice were normal.

3.5 Sample Preparation

50-100 µg of whole liver tissue was homogenized with a TissueLyser (Qiagen) in 400µl of ice cold lysis buffer (PBS, 4% sodium deoxycholate, 100mM DTT), incubated for 2-3 hr at 100°C, denaturated and reduced using the FASP Protein Digestion Kit (Expedeon Inc, Cat. No. 44250). Briefly, the samples were mixed with 0.3 ml of 8 M urea in 0.1 M Tris/HCl pH 8.5 (UA solution), loaded into the filtration devices, alkylated in 0.1 ml of 50 mM iodoacetamide in UA solution for 1 h in darkness at room temperature (RT). Samples were digested using sequentially 1 µg of LysC and 3 µg of Trypsin in 50 mM NaHCO3 solution at 37 °C overnight. Peptides were collected by centrifuging the filters at 20°C for 15 min at 14000 g and the devices were washed twice with 40 µl of 50 mM NaHCO3 and once with 50 µl of 0.5 M NaCl to eliminate the hydrophobic interaction with the filter. Each sample digest was desalted on StageTips and analyzed by liquid chromatography-tandem mass spectrometry (LC-MS/MS).

3.6 NanoLC setup

Peptide separation was performed with Dionex Ultimate 3000 RSLC nanoSystem. Samples were first loaded from the sample loop onto a trapping column (2 cm × 100 µm ID, Acclaim PepMap C18, 2 µm particles, 100 Å pore size; Thermo Scientific Cat. No. 164564) using the loading solvent (98% H2O and 2% CH3CN, 0.1% formic acid) at a flow rate of 5 µl/min for 5 min. The trapping column was then switched in-line with the separation column, and peptides were eluted with increasing organic solvent at a flow rate of 300 nl/min. The peptide separation was carried out using EASY-Spray column (25 cm x 75 µm ID, PepMap C18, 2 µm particles, 100 Å pore size; Themo Scientific Cat. No. ES803), mounted on the EASY Spray Ion Source, thermostated at 40 °C. Peptides were separated and eluted with a multi-steps gradient of 5–30% solution B (80% CH3CN and 20% H2O, 0.1% formic acid) in 170 min, 30-45% solution B in 35 min.

3.7 Mass spectrometer setup

The mass spectrometer LTQ-Orbitrap Velos Pro was operated in positive ionization mode. Single MS survey scans were performed in the Orbitrap, recording a mass range between 350-1650 m/z with a resolution of 60000. The

automatic gain control was set at 1.000.000 with a maximal ion injection time of 250 ms. The lock mass option was enabled allowing the internal recalibration of spectra recorded in the Orbitrap by polydimethylcyclosiloxane background ions (protonated (Si(CH3)2O)6); m/z 445.120025). The experiments were done in data-dependent acquisition mode with alternating MS and MS/MS experiments. The minimum MS signal for triggering MS/MS has been set to 3000 ions, with the most prominent ion signal selected for MS/MS using an isolation window of 2 Da. The m/z values of signals already selected for MS/MS were put on an exclusion list for 90 s using an exclusion window size of ±10 p.p.m. In all cases, one micro-scan was recorded. CID was done with a target value of 3,000 ions in the linear ion trap, a maximal ion injection time of 100 ms, normalized collision energy of 35%, a Q-value of 0.25 and an activation time of 10 ms. A maximum of 20 MS/MS experiments were triggered per MS scan.

3.8 Bioinformatics procedures and statistical analysis

The schematic representation of the bioinformatics analyses used in the present study is shown in Figure 1. Raw mass spectrometric data were analyzed with the MaxQuant software (version 1.5.3.30) (43). A false discovery rate (FDR) of 0.01 for proteins and peptides and a minimum peptide length of 6 amino acids were required. A time-dependent mass recalibration algorithm was used together with the Xcalibur lock mass option for recalibration to improve the mass accuracy of precursor ions (44). MS/MS spectra were searched by the Andromeda search engine, which is incorporated into the MaxQuant software suite (45) against Uniprot human database (release 2013_03) combined with 248 common contaminants and concatenated with the reversed versions of all sequences. The trypsin was chosen as enzyme specificity. Cysteine carbamidomethylation was selected as a fixed modification, while protein N-terminal acetylation, methionine oxidation and deamidation (N, Q), were selected as variable modifications. Maximally two missed cleavages were allowed. Initial mass deviation for the precursor ion was up to 7 ppm, and maximum allowed mass deviation for fragment ions was 0.5 Da. Quantification in MaxQuant was performed using the built-in label-free quantification algorithm (46), enabling the ‘Match between runs’ option (time window 2 minutes).

Comparative proteomics profiling was performed by Principal Component Analysis (PCA) implemented in ClustVis online resource (47). Time-course algorithm was used across the 6 experimental time points to identify differentially expressed proteins. Time-course analysis used the Significance Analysis of Microarrays method (48) implemented in the Web-enabled and Cross-platform SAM via Shiny (https://github.com/MikeJSeo/SAM). For building the SAM interactive web app straight from R, we used the Shiny R package setting up a two classes, unpaired, time course analysis with slope function as summary measure for each time course. The slope is useful for finding proteins with a consistent increase or decrease over time. For two class-unpaired data, SAM summarizes each time series by a slope. Then the slopes are compared across the two groups. Thus a positive SAM score means that the slopes are larger (on average) in the group 2 than in the group 1; the opposite is true for a negative. A positive SAM score could mean that the slopes are positive in both groups, but larger in the group 2, or they could both be negative but less negative in group 2, or finally they could be negative in group 1 and positive in group 2.

Gene ontology (GO) and KEGG analyses were carried out on selected groups of proteins using the STRING-DB software (49). An FDR lower than 0.05 identified significantly enriched ontology terms and pathways.

STRING-DB software was also used to evaluate protein-protein interaction (PPI) network from selected groups of proteins. PPI enrichment p value was used to assess whether a group of proteins have more interactions among themselves than what would be expected from a random set of proteins of similar size, drawn from the genome. We considered significantly a PPI enrichment p value lower than 0.05.

Statistical calculations were performed using Prism for Macintosh V6 (GraphPad Software Inc., La Jolla, CA).

3.9 Gene set enrichment analysis

We used GSEA (50) to evaluate the enrichment of known biological processes and pathways in LS-*G6pc*$^{-/-}$ mice. We carried out the analysis on all available protein symbols. GSEA calculates an enrichment score (ES) and normalized enrichment score (NES) for each gene set and estimates the statistical significance of the NES by an empirical permutation test using 1.000 gene permutations to

obtain the nominal p-value. However, when multiple gene sets are evaluated, GSEA adjusts the estimate of the significance level to account for multiple hypothesis testing. To this end, GSEA computes the False Discovery Rate q-value (FDR q-value) measuring the estimated probability that the normalized enrichment score represents a false positive finding (50). The gene sets used in the analysis belong to the Hallmark (H), KEGG (C2.CP.KEGG) and Gene Ontology (C5.GO) collections of the Molecular Signature Database (MSigDB) v6.2 database (51,52). A gene set with nominal p value lower than 0.05 and FDR q-value lower than 0.25 is considered significant.

3.10 Mouse plasma samples

Blood was collected from the heart at the time of the sacrifice, in EDTA tubes and was centrifuged at 2100 rpm for 10 minutes at room temperature (RT) to collect plasma. Plasma was stored at -80° C or used immediately for exosome isolation. The samples were collected at different time-points (1-3, 4-6, 7-9, 10-12, 13-15 months) that reflect different stages of disease progression.

3.11 Exosome isolation and miRNA purification from plasma

Exosomes isolation and RNA extraction were performed with the exoRNeasy Serum/Plasma Midi kit (Qiagen Italia, Milan, Italy). 100 µl of plasma were centrifuged at 16,000 x g at 4°C to eliminate cellular debris. Supernatants were then mixed with one volume of XBP binding buffer, loaded onto the exoEasy spin column, and spun at 500 x g 1 minute at RT. Next, 3.5 ml of XWP Washing Buffer was added to the filter column and spun at 5,000 x g for 5 minutes at RT. The spin column was transferred to a new collection tube and centrifuged at 5,000 x g for 5 minutes at RT after the addition of 700 µl of QIAzol to the membrane, to collect the lysate. Next, RNA extraction was performed according to the manufacturer's instructions. Quality control and miRNA evaluation were performed on the Agilent 2100 Bioanalyzer, using the Small RNA Assay (Agilent Technologies Spa, Cernusco sul Naviglio, Milan, Italy).

3.12 Quantitative Real Time PCR (qRT-PCR)

Exosomal miRNA were analyzed by the TaqMan Array Card Technology. miRNA were reverse transcribed with the TaqMan® microRNA Reverse Transcription Kit, using the Megaplex™ RT primers Rodent Pool A (Thermo Fisher Scientific, Monza, MB, Italy). Pre-amplification of cDNA was performed with TaqMan® PreAmp Master Mix and Megaplex™ Pre-Amp primers Rodent Pool A. The pre-amplification product was diluted according to the manufacturer's instructions and used to perform microRNA profiling on the ViiA™ 7 Real-Time PCR System. Briefly, 9 µl of the diluted pre-amplified product was mixed with 450 µl TaqMan® Universal Master Mix II, No UNG (Thermo Fisher Scientific, Monza, MB, Italy) and 441 µl of nuclease-free water. 100 µl of the PCR reaction mix was dispensed into each well of the TaqMan® Array Rodent microRNA A card (Thermo Fisher Scientific, Monza, MB, Italy), enabling the quantification of 381 miRNA.

3.13 Bioinformatic procedures and statistical analysis

We designed ExoPIPE, a new bioinformatic pipeline implemented in R, for the analysis of exosomal miRNA (exo-miR) expression measured by quantitative real-time PCR technology. The pipeline used functions implemented in both published R packages (53,54) and R modules implemented in our laboratory. ExoPIPE is composed by the following main modules: data preprocessing, Cycle Threshold (CT) filtering, data normalization, data imputation, and feature selection.

Data preprocessing module retrieves the tab separated text file containing CT values and any feature meta-data from every high-throughput qPCR experiment and creates a single raw data file containing the CT value of each well on the card, as well as information about the quality of the wells (e.g. experiment failure=TRUE/FALSE) (53). CT filtering module assigns a category (i.e. underdetermined, unreliable) to a CT value based on the different criteria and it filters out CT values based on their category (53). For instance, we categorized as unreliable any CT value higher than 32 in accordance with the literature (55), any CT value lower than 14, or undergoing an experiment failure as recommended by the manufacturer guidelines.

Data normalization module reduces unwanted technical variation in the data using different methods including rank invariant, geometric mean, and quantile (53). Global mean method (GM) is a normalization method, which uses the mean expression value of a sample as candidate normalizer (56). GM is a recognized method of normalization for microRNA RT-qPCR data, but it is not implemented in the HTqPCR package at the moment. So, we extended HTqPCR implementing GM to normalize exo-miR expression profiles. Cumulatitve distribution of miRNA coefficient of variation values and Kolmogorov-Smirnov test assessed the performance of the GM normalization, as it was already shown in the literature (56). Data imputation module filters out any miRNA whose expression was undetermined or unreliable (NA) for a pre-specified number of samples and imputes the remaining NAs with an appropriate method. Data filtering has a dedicated function in the HTqPCR package (53). Whereas, NA values were imputed with the lowest expression value of the respective miRNA minus one log2 unit (55). To maintain the bias introduced with imputation low, only exo-miRs detected in at least 95% of samples were included in the analysis.

RankProd R package (57) has been used to identify differentially expressed miRNAs. miRNA with fold change >1.5, p-value<0.05 and FDR<0.05 are considered significant.

4. RESULTS

4.1 Characterization of hepatic focal lesions in LS-*G6pc*$^{-/-}$ mice

LS-*G6pc*$^{-/-}$ mice livers were histologically examined. Liver parenchyma showed the classical histological features of GSD1a (20,22).

All HCA were histologically examined and immunostained for pathological classification. Histological analysis of HCA of LS-*G6pc*$^{-/-}$ mice showed that they were un-encapsulated nodules composed of hepatocytes with no or little atypia and with no or few intralesional portal tracts (Fig. 7A, a, d, and g).

Anti-GS, to identify bHCA, high risk adenomas, and anti-SAA antibodies, to identify IHCA, were used. For GS, only a strong and diffuse cytoplasmic staining was considered positive and staining intensity was comparable to the staining in normal liver in the centrilobular, perivenular hepatocytes. SAA marked both IHCA hepatocytes with granular cytoplasmic staining and amyloid deposits in vascular and/or sinusoidal spaces. We previously reported that 90% of LS-*G6pc*$^{-/-}$ mice develop amyloidosis by 12 months of age (22).

HNF1alpha-mutated HCA have not been identified in GSD-related HCA (19) and therefore silenced FABP1 was not searched for in LS-*G6pc*$^{-/-}$ mice liver tumors.

18 nodules stained positive for SAA and negative for GS, and were identified as IHCA (Fig. 7A,b and c), 8 nodules stained negative for SAA and positive for GS and were identified as high risk bHCA (Fig. 7A,e and f), and 12 nodules were negative for both SAA and GS and were classifies as UHCA (Fig. 7A,h and i). Moreover, three lesions were well differentiated HCC (Fig. 7B,a), characterized by positive staining for GS (Fig. 7B,b) and loss of reticulin framework (Fig. 7B,c). These results, summarized in Table 4, are in agreement with the molecular characterization of HCA in patients with GSD1a (19).

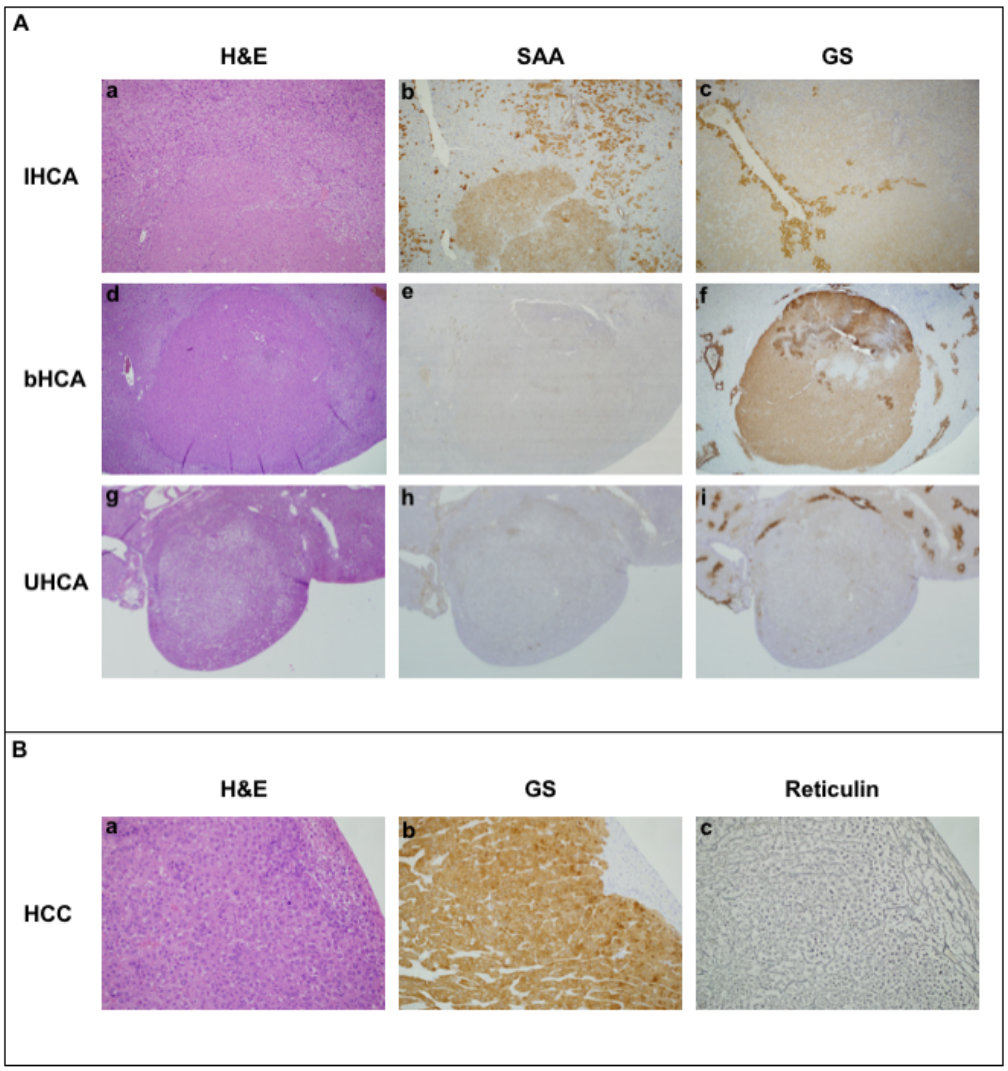

Figure 7. Immunoclassification of adenomas in LS-G6pc$^{-/-}$ mice. LS-G6pc$^{-/-}$ mice livers were fixed with 10% formalin and paraffin embedded. Serial sections were stained with hematoxilin/eosin (H&E) or treated with anti-serum amyloid (SAA) or anti-glutamine synthetase (GS) antibody. (**A)** Histological features and immunohistochemistry analysis of liver adenomas in LS-G6pc$^{-/-}$ mice. H&E-stained section of an IHCA **(a)**. An IHCA nodule shows diffuse positivity for SAA within the lesion, while the surrounding parenchyma is negative except for perivascular amyloid deposition (**b**). The same nodule shows negativity for GS antibody, while the surrounding non-lesional parenchyma shows normal GS staining in perivascular hepatocytes (**c**). H&E-stained section of a bHCA **(d)**. A bHCA nodule is negative for SAA (**e**) but shows strong positivity for GS within the lesion, while the surrounding non-lesional parenchyma shows normal zonation of expression in perivascular hepatocytes (**f**). H&E-stained section of an UHCA **(g)**. An UHCA nodule is negative for both SAA (**h**) and GS (**i**). (**a-c**): 10x magnification; (**d-i**): 4x magnification. (**B)** Histological features and immunoexpression of GS in a liver carcinoma. (**a**) H&E-stained section of a

nodule showing atypia. (**b**) Strong and diffuse positivity to GS within the lesion. (**c**) An HCC section stained with Gomori stain, showing loss of reticulin framework typical of malignancy. Reticulin is preserved in the surrounding parenchyma. (**a-c**): 20x magnification.

4.2 Correlation between MR signals and immunohistological analysis in livers of LS-*G6pc*$^{-/-}$ mice

To characterize the hepatic lesions detected in LS-*G6pc*$^{-/-}$ mice and correlate MRI features to the different adenoma subtypes, a total of 40 animals aged 13-18 months were scanned by 3 T clinical MRI and checked for focal lesions in all sequences acquired. A total number of 41 liver lesions were detected in 18 out of the 40 animals analyzed with an incidence of 45%. 25 mice were scanned once and sacrificed immediately after MRI acquisition. The remaining 15 mice were monitored every four weeks for three months to evaluate lesion growth and complication onset such as rupture and bleeding (see Table 2), as described below. MRI identified 4 different patterns of contrast uptake after contrast administration: isointense, very hyperintense, and very hypointense lesions, and lesions with a peripheral contrast enhancement.

All typical IHCA were isointense on pre-contrast T1-WI and on T2-WI (Fig. 8A and C). On T1-WI after contrast administration, 11/18 (61%) of the IHCA showed a very hyperintense signal compared to the surrounding liver (Fig. 8B), while 6/18 (33%) showed a peripheral rim of contrast enhancement and central hypointensity (Fig. 6D and E). We observed one case of adenoma (1/18, 6%) featuring high expression of both SAA and GS (data not shown). This lesion was isointense on pre-contrast T1-WI (Fig. 8D) and, after contrast administration, was hyperintense and characterized by the presence of a faint hypointense central scar (Fig. 8E and E'). On T2-WI, the lesion was hypointense while the central scar was hyperintense (Fig. 8F and F').

None of the bHCA, featuring GS overexpression, showed hyperintensity compared to the surrounding liver in the hepatocyte phase or peripheral rim of contrast enhancement after contrast sequences. 5/5 lesions (100%) were very hypointense after contrast administration on T1-WI and mildly hyperintense on T2-WI (Fig. 8G-I).

All well-differentiated HCC (3/3) were mildly hyperintense on T2-WI, isointense on T1-WI before contrast, and very hypointense (2/3) (Fig. 9J-L) or mildly hypo/isointense (1/3), after contrast administration (not shown).

UHCA showed all 4 different contrast enhancement patterns: the majority (7/12) were very hypointense lesions, 2/12 isointense, 1/12 very hyperintense and 2/12 with peripheral ring of contrast enhancement. Fig. 8M-O show representative images of a very hypointense UHCA lesion. All UHCA lesions were isointense on T2-WI (Fig. 8O), differently from bHCA and HCC, which are mildly hyperintense (Fig. 8I and L).

These results, summarized in Table 3, indicate that our MRI protocol can be used to identify HCA and to distinguish high-risk from low-risk adenomas. MRI could therefore represent a less invasive tool for early diagnosis and classification of HCA necessary for correct patient management.

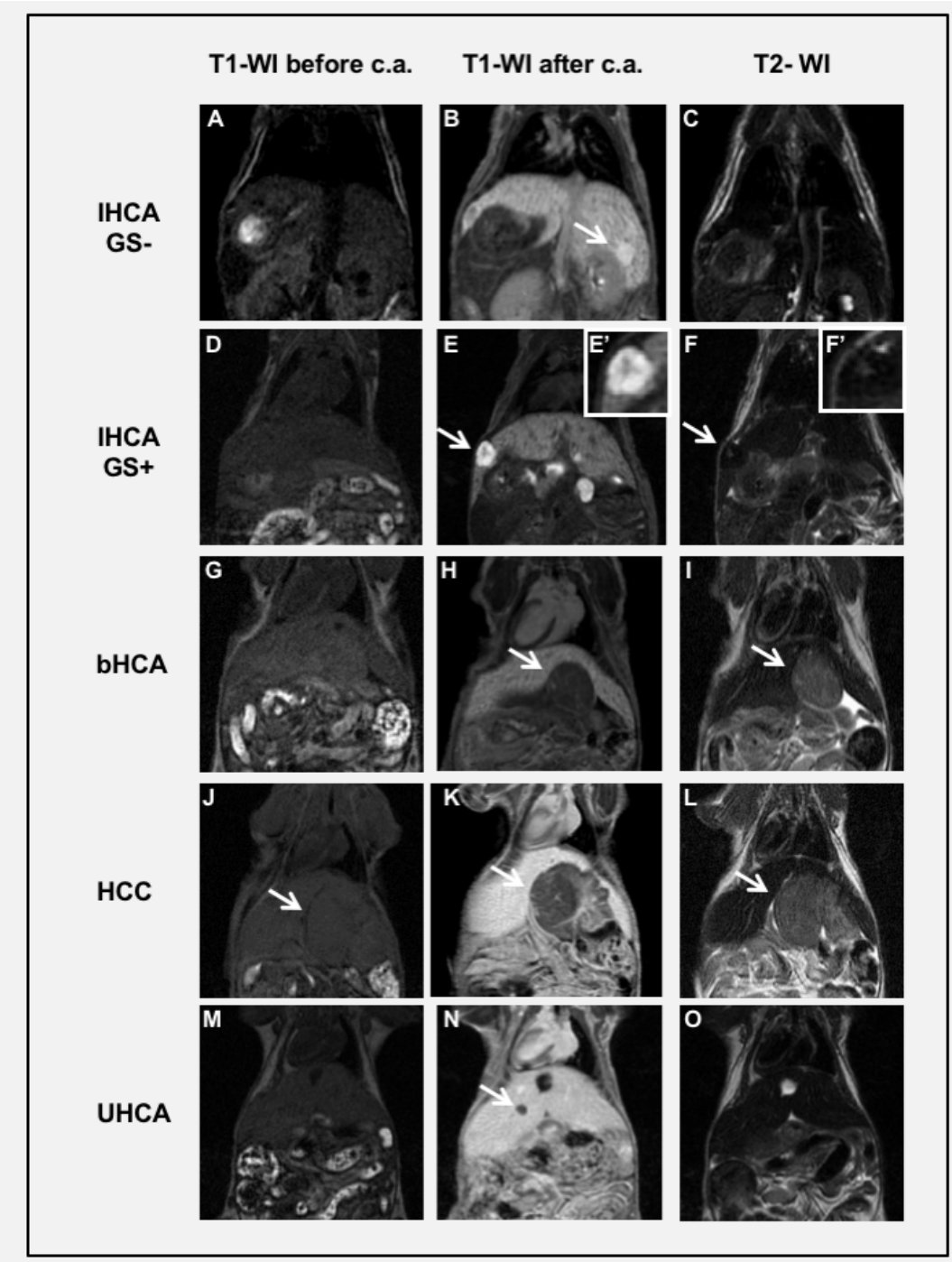

Figure 8. MRI of various subtypes of liver lesions in LS-G6pc$^{-/-}$ mice. LS-G6pc$^{-/-}$ mice were scanned by MRI and checked for focal lesions in all acquired sequences. (**A-C**) A typical IHCA is isointense on T1-WI, before contrast administration (c.a.) (**A**), and on T2-WI (**C**), while on T1-WI, after c.a., it shows areas of hyperintensity compared to the surrounding liver (**B**, arrow). (**D-F**) An atypic IHCA is isointense on T1-WI, before c.a., (**D**) but hyperintense, after c.a. (**E**, arrow) and characterized by the presence of a faint hypointense central scar (**E'**), mildly hyperintense on T2-WI (**F**, arrow and **F'**). (**G-I**). A bHCA lesion is isointense to the liver parenchyma on T1-WI before c.a. (**G**), hypointense on contrast enhanced T1-WI (**H**,

arrow) and mildly hyperintense on T2-WI (**I**, arrow). (**J-L**) The HCC shown is isointense on T1-WI acquired before c.a. (**J**, arrow), while it shows prominent hypointensity on T1-WI after c.a. (**K**, arrow) and slightly hyperintense on T2-WI (**L**, arrow). (**M-O**) A UHCA lesion is isointense on T1-WI before c.a. (**M**), hypointense on T1-WI, after c.a. (**N**, arrow). The nodule is isointense to the liver parenchyma on T2-WI, differently from bHCA, and HCC (**O**).

4.3 Monitoring of hepatic lesions

In order to characterize the evolution and growth of the liver lesions in LS-*G6pc*$^{-/-}$ mice, we performed periodic MRI on 15 LS-*G6pc*$^{-/-}$ mice aged 13-15 months. The animals were monitored every 4 weeks for three months and the tumor growth was analyzed by measuring lesion diameter using the off-line workstation. Tumor measurement was done on the basis of T1-weighted contrast-enhanced scans. Seven mice showed presence of nodules.

Time-dependent monitoring demonstrated that hyperintense lesions (n=4) on contrast enhanced T1-WI, without evidence of hyperintensity on T2-WI, had a slow growth rate. All these lesions were identified by immunohistochemistry as IHCA. A representative nodule is shown in Fig. 9.

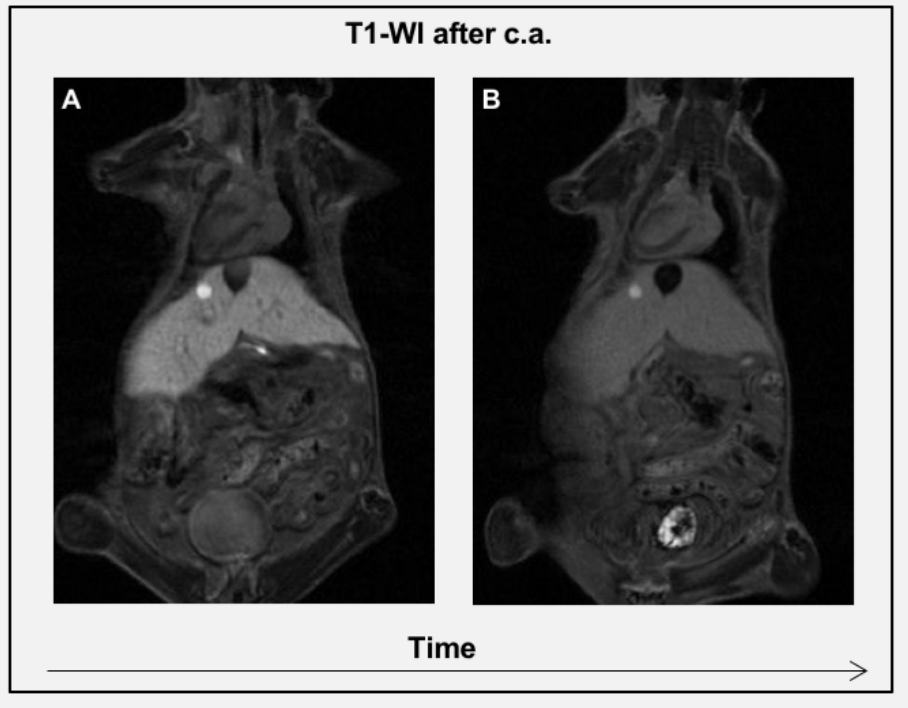

Figure 9. Growth characteristics of IHCA. Tumor measurement in LS-*G6pc*$^{-/-}$ mice was done on the basis of T1-weighted contrast-enhanced scans. (**A**) A hyper-intense lesion was detected on T1-WI after contrast administration (c.a.) at the first MRI evaluation. (**B**) One month later, the lesion had not changed in size and was classified as IHCA by immunohistochemistry.

At the first MRI evaluation one of these mice showed 2 very hypointense nodules on T1-WI after contrast administration (Fig. 10A). Interestingly, these 2 lesions showed different signals on T2-WI imaging: the smaller one was, at the first MRI examination, isointense (Fig. 10B, arrow) while the bigger one was mildly hyperintense (Fig. 10B, dashed arrow).

After one month, one of the lesions had only slightly changed in size (Fig. 10C, arrow) but had become mildly hyperintense on T2-WI (Fig. 10D, arrow), while the other lesion had significantly increased its size (Fig. 10C, dashed arrow), remaining hyperintense on T2-WI (Fig. 10D, dashed arrow) with an internal cystic degeneration.

At the third MRI evaluation, also the smaller lesion showed 50% increase in size, suggesting a fast growth rate (Fig. 10E, arrow). Both lesions remained mildly

hyperintense on T2-WI (Fig. 10F) and were classified by immunohistochemistry as UHCA.

These findings support the hypothesis that lesions hypointense on HPB phase and mildly hyperintense on T2-WI are rapidly growing tumors. This preliminary experiment underlies the need of further studied to better understand the real biological behavior of UHCA.

A third lesion, hyperintense on post contrast T1-WI (Fig. 10E, arrowhead) was visualized at this stage and characterized as an IHCA.

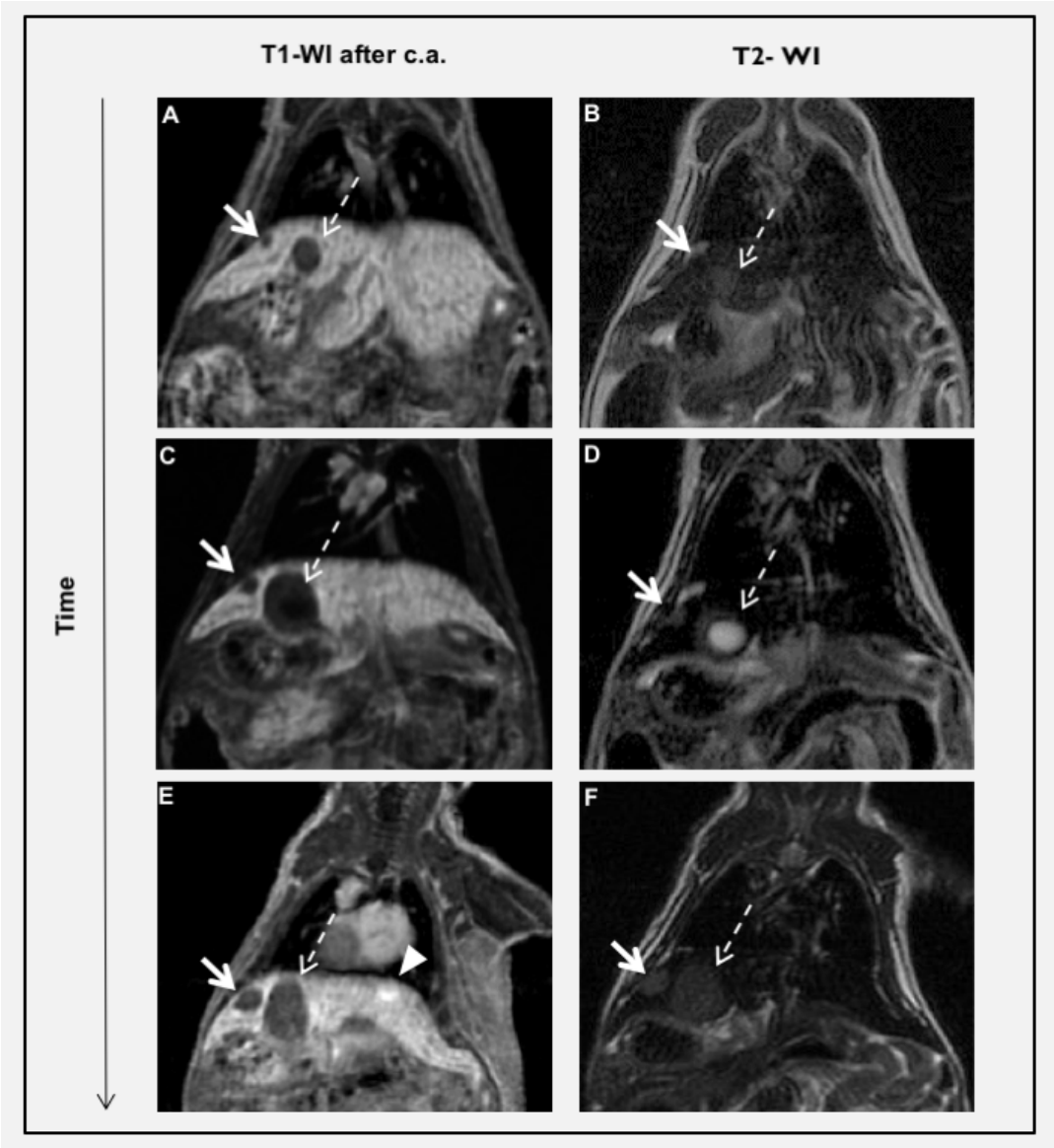

Figure 10. Time-dependent monitoring of hepatic lesions. LS-G6pc$^{-/-}$ mice were monitored every 4 weeks for three months and the tumor growth was analyzed by measuring lesion diameter using the off-line workstation. At the first MRI evaluation (**A,B**) 2 lesions were both hypointense on contrast enhanced T1-WI but showed different signals on T2-WI imaging:

the small nodule was hypointense (arrow) while the bigger nodule was hyperintense (dashed arrow). After one month (**C,D**), one lesions (arrow) had slightly changed in size and had become hyperintense on T2-WI, while the other lesion (dashed arrow) had rapidly increased in size and presented with a large central cystic portion that can denote a necrosis area (bright signal intensity). At the third MRI evaluation (**E,F**), also the small lesion (arrow) showed a size increase of 50%, suggesting a high growth rate. Both lesions were ipointense on T1-WI after c.a. and hyperintense on T2-WI. They were classified by immunohistochemistry as UHCA. A third lesion, hyperintense on contrast enhanced T1-WI (arrowhead) and isointense on T2-WI, was detected and identified as an IHCA.

4.4 Expression profiling of hepatic proteins in LS-*G6pc*$^{-/-}$ and WT mice

To identify potential biomarkers and key biological processes associated with liver degeneration in GSD-1a, we analyzed the proteomic expression profile of LS-*G6pc*$^{-/-}$ and wild type (WT) mice. The flowchart summarizing the main steps of these analyses is shown in Figure 11.

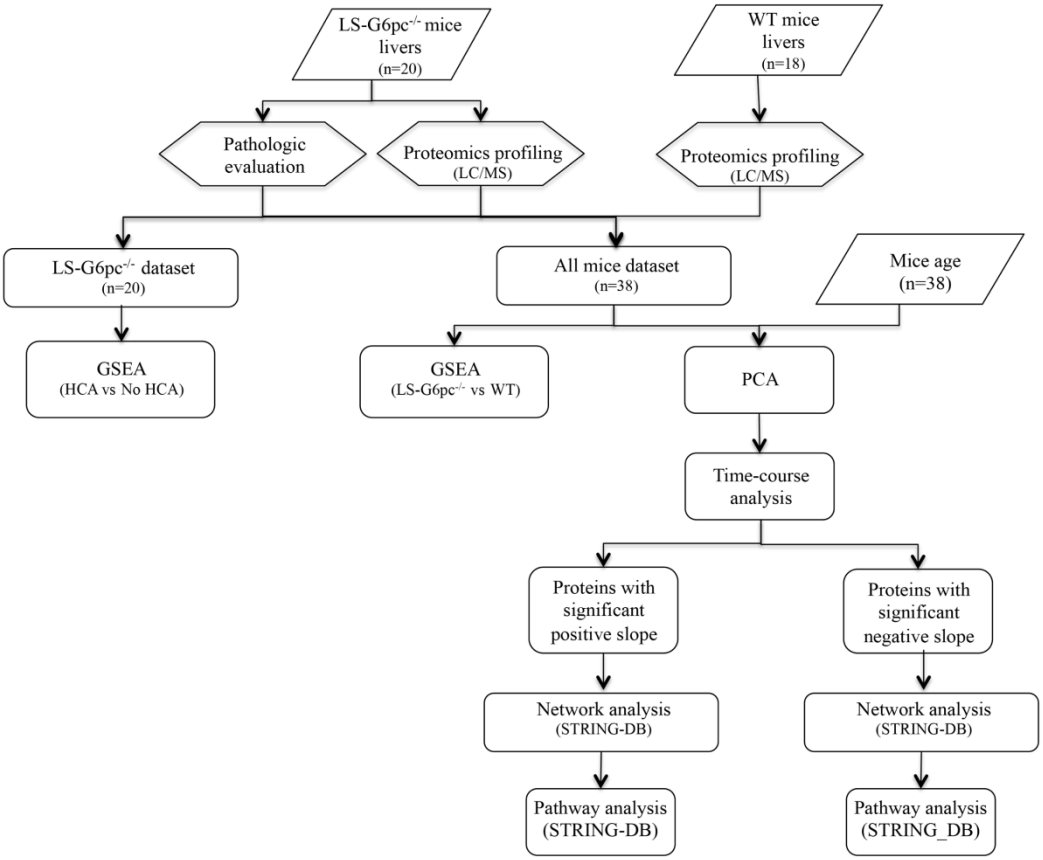

Figure 11. Schematic representation of the whole bioinformatic strategy used in the study

The protein expression profile of 18 WT and 20 LS-*G6pc*$^{-/-}$ mouse livers was measured by LC-MS/MS. Pathological evaluation of the livers assessed the presence of hepatic adenomas within the entire set of LS-*G6pc*$^{-/-}$ mice samples. Gene set enrichment analysis (GSEA) assessed the enrichment of curated protein-encoding gene sets in the groups of LS-*G6pc*$^{-/-}$ mice characterized by the presence\absence of hepatic adenomas, and in the groups of mice characterized by the presence\absence of GSD-1a disease. The expression profile of LS-*G6pc*$^{-}$

$^{-/-}$ and WT mice over 6 distinct age groups was compared using SAM. Analysis identified two sets of differentially expressed proteins including proteins with a significant positive and proteins with a significant negative slope. The two sets of significantly differentially expressed proteins were used for network and pathway analyses. Network analysis evaluated the presence of a potential functional connection among the significant proteins. Pathway analysis identified the most significantly altered biological processes and pathways.

Mice were divided into six groups according to their age (Table 5). A total of 20 LS-*G6pc*$^{-/-}$ and 18 WT mice were analyzed. All LS-*G6pc*$^{-/-}$ mice utilized were characterized for pathological manifestations and found to display all the features already described for this murine model of GSD-1a (22), including hepatomegaly and glycogen accumulation (data not shown). Six LS-*G6pc*$^{-/-}$ mice developed at least one HCA. None of the WT mice developed liver disease, as expected.

Livers were profiled by a proteomic approach based on high-resolution mass spectrometry (HRMS) coupled with liquid chromatography techniques. We obtained a total of 57893 peptides that mapped to 4763 unique mouse gene symbols. Of these, 4138 significantly expressed proteins were quantified and organized in a dataset.

Group	Age (months)	LS-*G6pc*$^{-/-}$	HCA	WT	HCA
1	1-3	3	0	3	0
2	4-6	3	0	3	0
3	7-9	3	0	3	0
4	10-12	3	1	3	0
5	13-15	3	3	3	0
6	16-18	5	2	3	0

Table 5 - Animals analyzed. Data are relative to the 20 LS-*G6pc*$^{-/-}$ mice and 18 wild type mice in the data set.

4.5 GSEA reveals the enrichment of hypoxia-related proteins in the expression profile of LS-*G6pc*$^{-/-}$ mouse livers

Gene set enrichment analysis (GSEA) (50) is a computational technique that determines whether an a priori defined set of genes (gene set) shows statistically significant concordant expression differences between two biological states. Seven distinct collections of gene sets are publicly available in MSigDB database (51,52). We carried out GSEA between 20 LS-*G6pc*$^{-/-}$ and 18 WT protein expression profiles using the hallmark collection composed by 50 curated gene sets that represent well-defined biological states or processes, the C5.BP collection composed by 4436 gene sets derived from Gene Ontology database, and the C2.CP.KEGG collection composed by 186 gene sets derived from the KEGG pathway database. To use MSigDB collections, protein symbols have been converted into the corresponding gene symbols. GSEA identified 71 significantly unregulated gene sets in the expression profile of the LS-*G6pc*$^{-/-}$ compared to WT groups of mice (Nom p-value<0.05 and FDR q-value < 0.25, data not shown). The list included gene sets related to the response to hypoxia and GSD-1a disease such as HALLMARK_HYPOXIA, HALLMARK_GLYCOLYSIS, and KEGG_ PYRUVATE_METABOLISM, GO_FATTY_ACID_BIOSYNTHETIC_PROCESS, and GO_GLUCOSE_6_PHOSPHATE_METABOLIC_PROCESS.

HALLMARK_HYPOXIA was the most significant hypoxia related gene sets (NES 2.07, Nom p- value=0.0 and FDR q-value=0.001, data not shown). The enrichment plot (Figure 12A) and the heat map (Figure 12B) show a graphical view of the enrichment score and the proteins expression value of the HALLMARK_ HYPOXIA gene set between the LS-*G6pc*$^{-/-}$ and the WT groups of mice. Among the 24 genes that mostly contributed to the enrichment of the HALLMARK_HYPOXIA gene set (leading edge subset), several enzymes involved in the lactic acid production by anaerobic glycolysis are upregulated in the livers of LS-G6pc$^{-/-}$ mice, such as PFKL, TPI1, GAPDH, PKLR, LDHA and PDK1.

These findings indicate that LS-*G6pc*$^{-/-}$ livers exhibit a hypoxic phenotype.

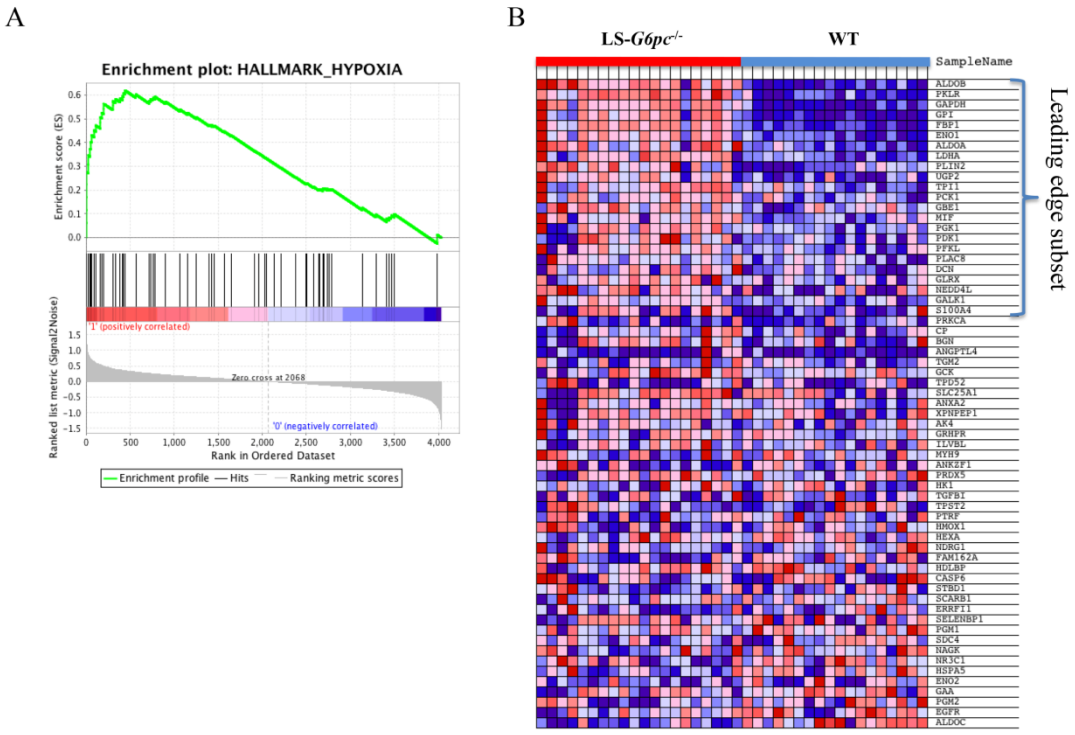

Figure 12. GSEA of HALLMARK_HYPOXIA gene set in LS-*G6pc*$^{-/-}$ mice

(A) Enrichment plot of the HALLMARK_HYPOXIA gene set showing the hypoxic phenotype of LS-*G6pc*$^{-/-}$ mouse liver. To use MSigDB collections, protein symbols have been converted into the corresponding gene symbols. Genes were ranked by level of up or downregulation comparing 20 LS-*G6pc*$^{-/-}$ and 18 WT mice. The enrichment score is calculated by walking down a list of genes ranked by their correlation with the phenotype, increasing a running sum statistic when a gene in that gene set is encountered (each black vertical line underneath the enrichment plot) and decreasing it when a gene that isn't in the gene set is encountered. The enrichment score is the maximum deviation from zero encountered in the walk. (B) Heat map visualization of the proteins belonging to the HALLMARK_HYPOXIA gene set showing a clear differential expression of the leading edge subset between LS-*G6pc*$^{-/-}$ and WT mice. The genes that mostly contributed to the enrichment of a gene set, named leading edge subset, are indicated by brackets. A gene set with nominal p value lower than 0.05 and FDR q-value lower than 0.25 was considered significantly enriched.

4.6. Time-course analysis highlights age-dependent modulation of protein expression in LS-*G6pc*$^{-/-}$ mouse livers

Age dependent modulation of protein expression may be instrumental to find biomarkers of LS-*G6pc*$^{-/-}$ mouse liver disease. We carried out Principal Component Analysis (PCA) of the proteomic profile of LS-*G6pc*$^{-/-}$ and WT mice grouped by age to highlight any similarities or differences between them (Figure 13). PCA revealed a clear separation between LS-*G6pc*$^{-/-}$ and WT mice in all age groups. Furthermore, we observed modulation of the proteomic profiles of both LS-*G6pc*$^{-/-}$ and WT mice across age groups.

Significance Analysis of Microarrays (SAM) is a statistical technique to perform differential expression analysis on different kinds of data including time-course data. Analysis summarizes each time course by a slope and treats the summarized data in the same way as it treats a two-class differential expression problem. The slope analysis is useful for finding proteins with a consistent increase or decrease expression over time on the basis of a delta value. Different delta values are associated with different false discovery rates (FDR) by SAM. We used the expression profile of LS-*G6pc*$^{-/-}$ and WT mice grouped by age to perform a time-course analysis using SAMR. We set up a delta value of 0.49 to maintain the false discovery rate below 15%. SAM analysis identified 1243 proteins with a significant differential slope between LS-*G6pc*$^{-/-}$ and WT mice. Among these proteins, 701 had a positive slope in LS-*G6pc*$^{-/-}$ (Score (d)>0 and q-value (%)<15) and 542 had a negative slope in LS-*G6pc*$^{-/-}$ with respect to WT mice (Score (d)<0 and q-value (%)<15 (Figure 14A). Heat map evidenced a clear opposite expression trend of these proteins as mice grew older, suggesting an age- dependent alteration of these proteins in LS-*G6pc*$^{-/-}$ mice and validating in such a way the results of the differential expression analysis (Figure 14B).

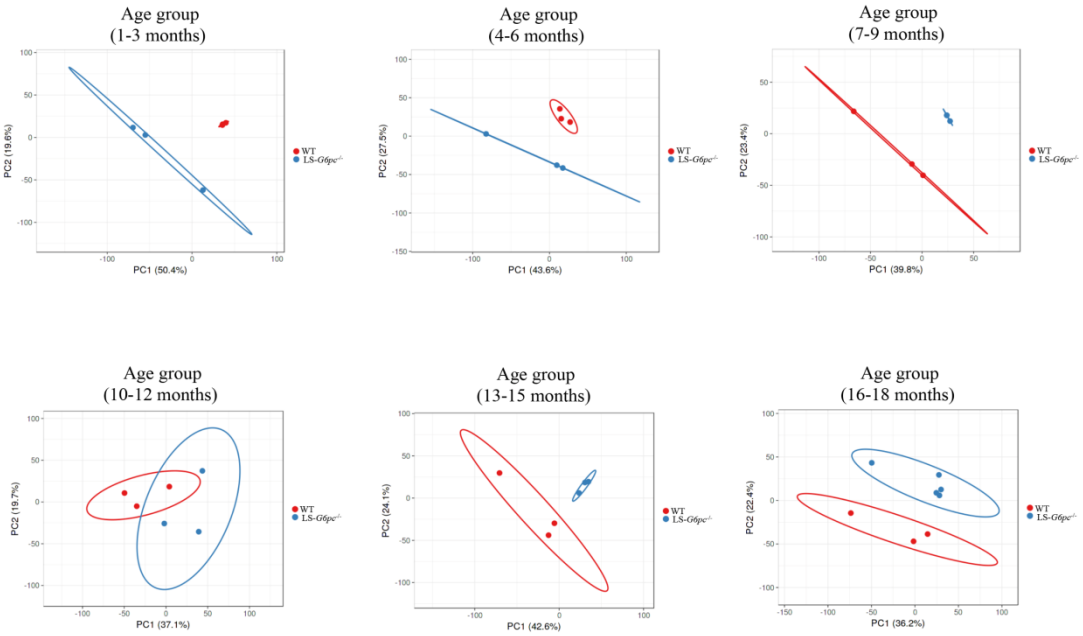

Figure 13. PCA of the LS-*G6pc*$^{-/-}$ and WT mice grouped by age

An age group defines a subset of mice of a pre-specified range of ages expressed in months. Each plot identifies a distinct age group. PCA used the whole proteomic profile of each sample. Axes in the PCA plot are relative to the two principal components with the largest variance. Ellipse around a group of samples indicates the estimated region where a new observation from that group would fall in with a certain probability (i.e. 95%). Each point indicates a sample and is labeled with the sample identifier. LS-*G6pc*$^{-/-}$ and WT mice are colored in blue or red, respectively.

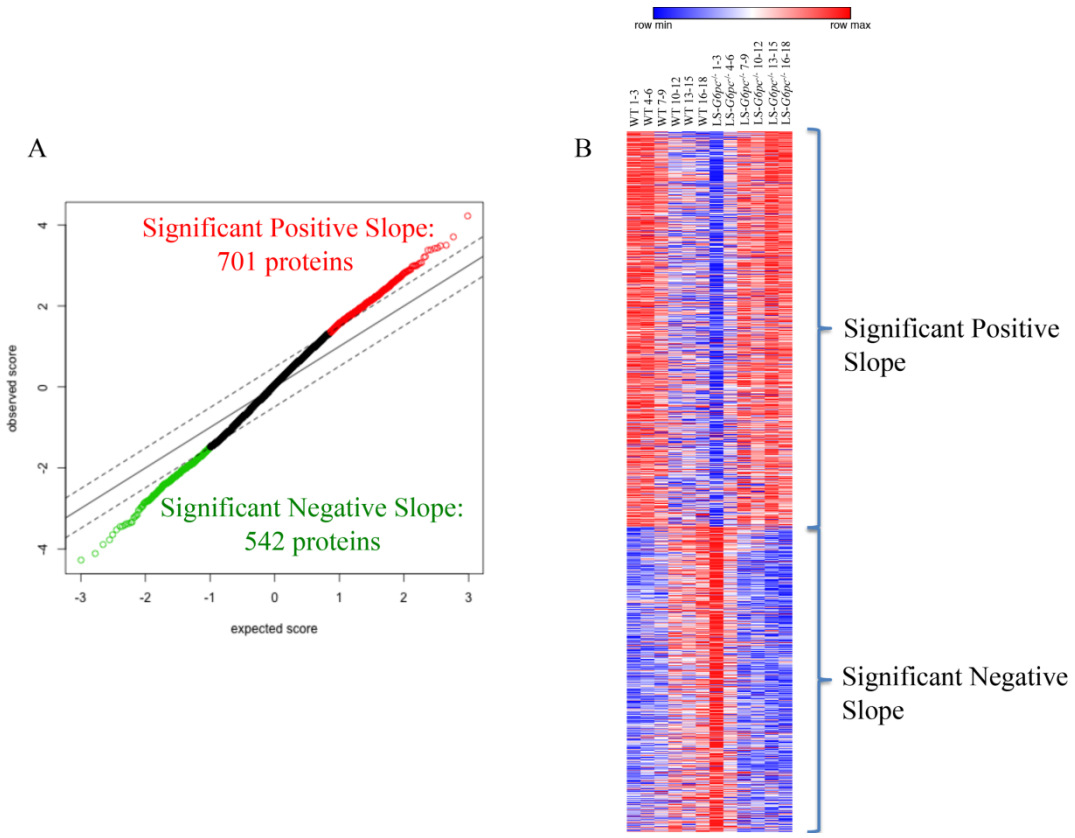

Figure 14. Time course analysis reveals an age dependent modulation of protein expression

(A) SAM plot generated by SAM tool in the time course analysis. A delta value of 0.49 was applied to identify significant differentially expressed proteins. Significant positive slope proteins are illustrated in red and significant negative slope proteins are depicted in green.

(B) Heat map of the significant differentially expressed proteins between LS-*G6pc*$^{-/-}$ and WT mice (lines) grouped by age and mouse type (columns). For each protein, mouse model type, and age group, the heat map displays the average expression of the protein among the samples of that particular type and age group. The expression data of each protein have been scaled and are represented by pseudo-colors. Red color corresponds to high level of expression and blue color corresponds to low level of expression. Brackets depict significant positive and negative slope proteins.

4.7. Network and pathway analyses reveal activation of specific biological processes associated with increased progression of liver disease

Network analysis can help to identify biologically relevant substructures within a group of proteins (49). We carried out a network analysis using STRING-DB based on the proteins identified in SAM analysis. Displaying a protein as a node and a functional association between two proteins as an edge, we built one network for the proteins with a significant positive slope and another network for the proteins with a significant negative slope. Visual inspection of the network for the proteins with a significant positive slope identified one dense cluster connecting the majority of the proteins in this group (Figure 15A), whereas, inspection of the network of proteins with a significant negative slope identified several sparse, but connected, clusters linking a restricted number of proteins (Figure 15B).

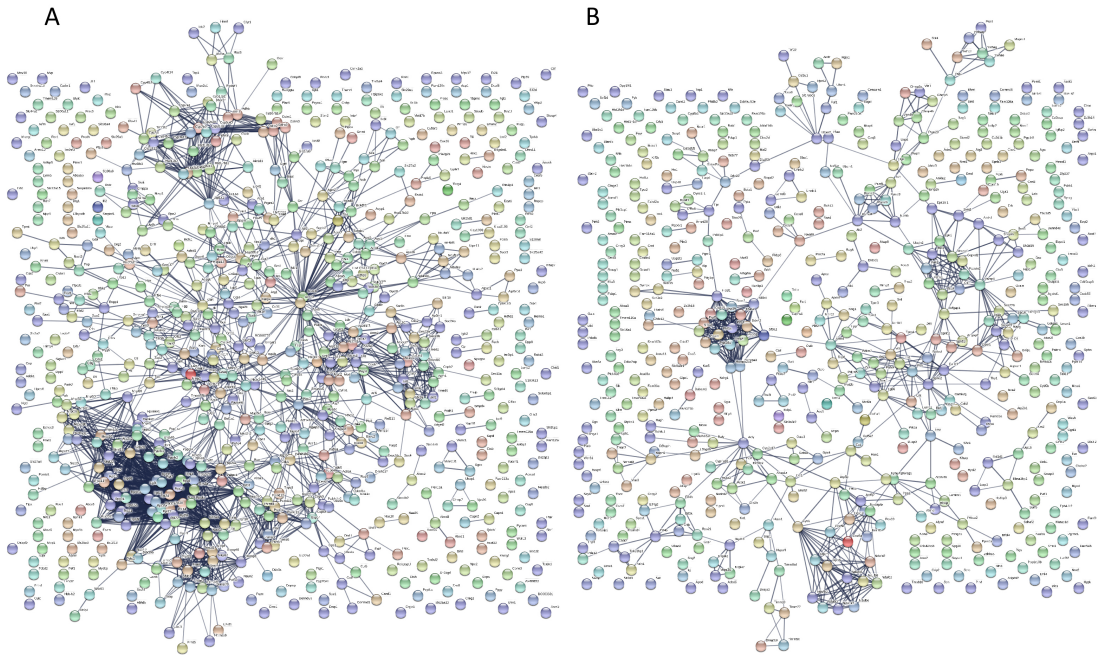

Figure 15. Association network of the proteins identified with the time-course analysis. The plot was generated by STRING-DB software. A network node represents a protein. An edge between two proteins represents the predicted functional association between them.

Associations are derived from high-throughput experimental data, from the mining of databases and literature, and from predictions based on genomic context analysis. The thickness of the line indicates the degree of confidence prediction of the association. Only associations with a high degree of confidence of 0.7 are displayed in the plot. (A) Association network among proteins with a significant positive slope. (B) Association network among proteins with a significant negative slope. The association between two proteins can mean direct physical binding, but can also mean indirect interaction such as participation in the same metabolic pathway or cellular process. Thus, the presence of clusters of associations suggests a functional connection among the proteins identified in the time-course analysis.

These results highlighted the presence of two distinct networks of proteins characterized by a different number of clusters and density. Both networks exhibited significantly more interactions than expected by chance (Protein-protein interaction enrichment p-value < 1.0e-16) suggesting a potential biological link among subsets of proteins identified in the SAM analysis.

We performed a pathway analysis on the two lists of proteins using STRING-DB to assess this biological connection. Pathway analysis based on Gene Ontology processes and KEGG pathways showed a significant enrichment of 451 GO biological processes and 107 KEGG pathways (data not shown). In particular, we observed an enrichment of proteins involved in non-alcoholic fatty liver disease, mitochondrial activity, inflammation response, and immune response (FDR q-value<0.05, Table 6), indicating that, as LS-*G6pc*$^{-/-}$ mice grew older, activation of specific biological processes associated with increased progression of liver disease occurred.

Biological process[a]	Gene set id[b]	Pathway or process description[c]	Number of proteins[d]	FDR q-value[e]	Slope[f]	Ontology[g]
Non-alcoholic fatty liver disease						
	GO.0006695	cholesterol biosynthetic process	9	1,96E-05	Positive	GO BP
	GO.0006805	xenobiotic metabolic process	13	1,77E-06	Positive	GO BP
	GO.0006631	fatty acid metabolic process	44	1,87E-18	Positive	GO BP
	GO.0006633	fatty acid biosynthetic process	20	3,04E-09	Positive	GO BP
	4910	Insulin signaling pathway	11	0,0125	Positive	KEGG
	3320	PPAR signaling pathway	16	6,12E-08	Positive	KEGG
	4152	AMPK signaling pathway	11	0,00852	Positive	KEGG
	190	Oxidative phosphorylation	16	8,92E-06	Negative	KEGG
	4932	Non-alcoholic fatty liver disease (NAFLD)	15	0,000158	Negative	KEGG
Mitochondrion						
	GO.0032543	mitochondrial translation	9	9,37E-05	Positive	GO BP
	GO.0007005	mitochondrion organization	24	0,00119	Positive	GO BP
	GO.0006637	acyl-CoA metabolic process	9	0,00267	Positive	GO BP
	GO.0042775	mitochondrial ATP synthesis coupled electron transp	5	0,00862	Negative	Go BP
	10	Glycolysis / Gluconeogenesis	9	0,00106	Positive	KEGG
	GO.0032981	mitochondrial respiratory chain complex I assembly	4	0,0399	Negative	GO BP
Inflammation						
	GO.0006953	acute-phase response	8	0,0011	Positive	GO BP
	GO.0002526	acute inflammatory response	10	0,00205	Positive	GO BP
	GO.0019373	epoxygenase P450 pathway	6	0,000793	Positive	GO BP
	GO.0070670	response to interleukin-4	8	0,000329	Positive	GO BP
	GO.0006958	complement activation, classical pathway	10	3,55E-07	Positive	GO BP
	4920	Adipocytokine signaling pathway	7	0,0206	Positive	KEGG
	4370	VEGF signaling pathway	7	0,0101	Positive	KEGG
Immune response						
	GO.0045087	innate immune response	25	0,00495	Positive	GO BP
	GO.0002252	immune effector process	22	0,00727	Positive	GO BP
	GO.0002682	regulation of immune system process	50	0,00502	Positive	GO BP
	GO.0002460	adaptive immune response based on somatic recombination of immune receptors built from immunoglobulin superfamily domains	12	0,00592	Positive	GO BP
	GO.0002684	positive regulation of immune system process	33	0,0119	Positive	GO BP
	4650	Natural killer cell mediated cytotoxicity	9	0,0256	Positive	KEGG
	4610	Complement and coagulation cascades	14	1,48E-06	Positive	KEGG

Table 6. Summary of the biological processes and pathways significantly modulated over time. [a]Concise names summarizing a group of significant GO biological processes and KEGG pathways. GO and KEGG enrichemnt analysis was carried outon proteins whose slope of expression in LS-*G6pc*$^{-/-}$ compared with WT mice was significantly modulated.

[b]Official identifier of a GO biological process or KEGG pathway.

[c]Official name of a GO biological process or KEGG pathway.

[d]Number of proteins of a GO biological process or KEGG pathway whose slope of expression was significantly modulated in LS-*G6pc*$^{-/-}$.

[e]FDR q-value estimates the significance of the enrichemnt of a biological process or a pathway. FDR q-value <= 0.05 are considered acceptable.

[f] Positive or Negative indicates the type of slope of the protein involved in a process or a pathway.

[g] Name of the ontology defining a biological process or pathway. GO BP stands for gene ontology biological process. KEGG stands for Kyoto Encyclopedia of Genes and Genomes.

Among the proteins with a significant slope in LS-*G6pc*$^{-/-}$ mice, we observed modulation of several proteins involved in glucose and lipid metabolism. While some of these proteins are consistent with an enhanced hepatic glycolytic pathway, others are consistent with an enhanced gluconeogenesis, suggesting that both metabolic pathways are activated. Compared to control mice, livers of older LS-*G6pc*$^{-/-}$ mice display downregulation of several components of oxidative phosphorylation (OXPHOS) process (both of the respiratory chain complexes and ATP synthase), and upregulation of several proteins involved in fatty acid and cholesterol biosynthesis. In addition, older LS-*G6pc*$^{-/-}$ mice show upregulation of aconitase, amino transferase (AT) and isocitrate dehydrogenase (IDH1) involved in 2-oxocarboxylic metabolism (Table 7).

Protein[a]	Approved name[b]	Slope[c]	Metabolism[d]
Aco1	Cytoplasmic aconitate hydratase (Aconitase) (EC 4.2.1.3) (Citrate hydro-lyase) (Iron regulatory protein 1) (IRP1) (Iron-responsive element-binding protein 1) (IRE-BP 1)	Positive	2-Oxocarboxylic acid metabolism
Got2	Aspartate aminotransferase, mitochondrial (mAspAT) (EC 2.6.1.1) (EC 2.6.1.7) (Fatty acid-binding protein) (FABP-1) (Glutamate oxaloacetate transaminase 2) (Kynurenine aminotransferase 4) (Kynurenine aminotransferase IV) (Kynurenine--oxoglutarate transaminase 4) (Kynurenine--oxoglutarate transaminase IV) (Plasma membrane-associated fatty acid-binding protein) (FABPpm) (Transaminase A)	Positive	2-Oxocarboxylic acid metabolism
Gpt	Alanine aminotransferase 1 (ALT1) (EC 2.6.1.2) (Glutamate pyruvate transaminase 1) (GPT 1) (Glutamic-alanine transaminase 1) (Glutamic-pyruvic transaminase 1)	Positive	2-Oxocarboxylic acid metabolism
Idh1	Isocitrate dehydrogenase [NADP] cytoplasmic (IDH) (EC 1.1.1.42) (Cytosolic NADP-isocitrate dehydrogenase) (IDP) (NADP(+)-specific ICDH) (Oxalosuccinate decarboxylase)	Positive	2-Oxocarboxylic acid metabolism
Pdk1	[Pyruvate dehydrogenase (acetyl-transferring)] kinase isozyme 1, mitochondrial (EC 2.7.11.2) (Pyruvate dehydrogenase kinase isoform 1) (PDH kinase 1)	Positive	Aerobic fate of pyruvate
Ldha	L-lactate dehydrogenase A chain (LDH-A) (EC 1.1.1.27) (LDH muscle subunit) (LDH-M)	Positive	Anaerobic fate of pyruvate
FDPS	farnesyl diphosphate synthase	Positive	cholesterol biosynthesis
HSD17B7	hydroxysteroid 17-beta dehydrogenase 7	Positive	cholesterol biosynthesis
IDI1	isopentenyl-diphosphate delta isomerase 1	Positive	cholesterol biosynthesis
MVD	mevalonate diphosphate decarboxylase	Positive	cholesterol biosynthesis
Mvd	Diphosphomevalonate decarboxylase (EC 4.1.1.33) (Mevalonate (diphospho)decarboxylase) (MDDase) (Mevalonate pyrophosphate decarboxylase)	Positive	cholesterol biosynthesis
TM7SF2	transmembrane 7 superfamily member 2	Positive	cholesterol biosynthesis
Hmgcs1	Hydroxymethylglutaryl-CoA synthase, cytoplasmic (HMG-CoA synthase) (EC 2.3.3.10) (3-hydroxy-3-methylglutaryl coenzyme A synthase)	Positive	cholesterol biosynthesis
Acaca	Acetyl-CoA carboxylase 1 (ACC1) (EC 6.4.1.2) (ACC-alpha) (Acetyl-CoA carboxylase 265) [Includes: Biotin carboxylase (EC 6.3.4.14)]	Positive	Fatty acid biosynthesis
Acacb	Acetyl-CoA carboxylase 2 (EC 6.4.1.2) (ACC-beta) [Includes: Biotin carboxylase (EC 6.3.4.14)]	Positive	Fatty acid biosynthesis
Fasn	Fatty acid synthase (EC 2.3.1.85) [Includes: [Acyl-carrier-protein] S-acetyltransferase (EC 2.3.1.38); [Acyl-carrier-protein] S-malonyltransferase (EC 2.3.1.39); 3-oxoacyl-[acyl-carrier-protein] synthase (EC 2.3.1.41); 3-oxoacyl-[acyl-carrier-protein] reductase (EC 1.1.1.100); 3-hydroxyacyl-[acyl-carrier-protein] dehydratase (EC 4.2.1.59); Enoyl-[acyl-carrier-protein] reductase (EC 1.3.1.39); Oleoyl-[acyl-carrier-protein] hydrolase (EC 3.1.2.14)]	Positive	Fatty acid biosynthesis
Acsl3	Long-chain-fatty-acid--CoA ligase 3 (EC 6.2.1.3) (Long-chain acyl-CoA synthetase 3) (LACS 3)	Positive	Fatty acid metabolism
Acsl4	Long-chain-fatty-acid--CoA ligase 4 (EC 6.2.1.3) (Long-chain acyl-CoA synthetase 4) (LACS 4) (mACS4)	Positive	Fatty acid metabolism
Acsl5	Long-chain-fatty-acid--CoA ligase 5 (EC 6.2.1.3) (Long-chain acyl-CoA synthetase 5) (LACS 5)	Positive	Fatty acid metabolism
Elovl1	Elongation of very long chain fatty acids protein 1 (EC 2.3.1.199) (3-keto acyl-CoA synthase Elovl1) (ELOVL fatty acid elongase 1) (ELOVL FA elongase 1) (Very long chain 3-ketoacyl-CoA synthase 1) (Very long chain 3-oxoacyl-CoA synthase 1)	Positive	Fatty acid metabolism
Elovl2	Elongation of very long chain fatty acids protein 2 (EC 2.3.1.199) (3-keto acyl-CoA synthase Elovl2) (ELOVL fatty acid elongase 2) (ELOVL FA elongase 2) (Very long chain 3-ketoacyl-CoA synthase 2) (Very long chain 3-oxoacyl-CoA synthase 2)	Positive	Fatty acid metabolism
Elovl5	Elongation of very long chain fatty acids protein 5 (EC 2.3.1.199) (3-keto acyl-CoA synthase Elovl5) (ELOVL fatty acid elongase 5) (ELOVL FA elongase 5) (Very long chain 3-ketoacyl-CoA synthase 5) (Very long chain 3-oxoacyl-CoA synthase 5)	Positive	Fatty acid metabolism
Fads2	Fatty acid desaturase 2 (EC 1.14.19.-) (Delta(6) fatty acid desaturase) (D6D) (Delta(6) desaturase) (Delta-6 desaturase)	Positive	Fatty acid metabolism
Scd1	Acyl-CoA desaturase 1 (EC 1.14.19.1) (Delta(9)-desaturase 1) (Delta-9 desaturase 1) (Fatty acid desaturase 1) (Stearoyl-CoA desaturase 1)	Positive	Fatty acid metabolism
Slc27a2	Very long-chain acyl-CoA synthetase (VLACS) (VLCS) (EC 6.2.1.-) (Fatty acid transport protein 2) (FATP-2) (Fatty-acid-coenzyme A ligase, very long-chain 1) (Long-chain-fatty-acid--CoA ligase) (EC 6.2.1.3) (Solute carrier family 27 member 2) (THCA-CoA ligase) (Very long-chain-fatty-acid-CoA ligase)	Positive	Fatty acid metabolism
Slc27a4	Long-chain fatty acid transport protein 4 (FATP-4) (Fatty acid transport protein 4) (EC 6.2.1.-) (Solute carrier family 27 member 4)	Positive	Fatty acid metabolism
Fbp1	Fructose-1,6-bisphosphatase 1 (FBPase 1) (EC 3.1.3.11) (D-fructose-1,6-bisphosphate 1-phosphohydrolase 1) (Fructose-1,6-bisphosphatase isozyme 3) (FBPase 3) (Liver FBPase)	Positive	Gluconeogenesis
Pck1	Phosphoenolpyruvate carboxykinase, cytosolic [GTP] (PEPCK-C) (EC 4.1.1.32)	Positive	Gluconeogenesis
Pck2	Phosphoenolpyruvate carboxykinase [GTP], mitochondrial (PEPCK-M) (EC 4.1.1.32)	Positive	Gluconeogenesis
Gck	Glucokinase (EC 2.7.1.2) (Hexokinase type IV) (HK IV) (Hexokinase-4) (HK4) (Hexokinase-D)	Positive	Glycolysis
Pfkl	ATP-dependent 6-phosphofructokinase, liver type (ATP-PFK) (PFK-L) (EC 2.7.1.11) (6-phosphofructokinase type B) (Phosphofructo-1-kinase isozyme B) (PFK-B) (Phosphohexokinase)	Positive	Glycolysis
Pklr	Pyruvate kinase PKLR (EC 2.7.1.40) (L-PK) (Pyruvate kinase isozymes L/R)	Positive	Glycolysis
Tpi1	Triosephosphate isomerase (TIM) (EC 5.3.1.1) (Triose-phosphate isomerase)	Positive	Glycolysis / Gluconeogenesis
Bpgm	Bisphosphoglycerate mutase (BPGM) (EC 5.4.2.4) (2,3-bisphosphoglycerate mutase, erythrocyte) (2,3-bisphosphoglycerate synthase) (EC 5.4.2.11) (BPG-dependent PGAM)	Positive	Glycolysis and gluconeogenesis
Gapdh	Glyceraldehyde-3-phosphate dehydrogenase (GAPDH) (EC 1.2.1.12) (Peptidyl-cysteine S-nitrosylase GAPDH) (EC 2.6.99.-)	Positive	Glycolysis and gluconeogenesis
Gpi	Glucose-6-phosphate isomerase (GPI) (EC 5.3.1.9) (Autocrine motility factor) (AMF) (Neuroleukin) (NLK) (Phosphoglucose isomerase) (PGI) (Phosphohexose isomerase) (PHI)	Positive	Glycolysis and gluconeogenesis
Cpt1a	Carnitine O-palmitoyltransferase 1, liver isoform (CPT1-L) (EC 2.3.1.21) (Carnitine O-palmitoyltransferase I, liver isoform) (CPT I) (CPTI-L) (Carnitine palmitoyltransferase 1A)	Positive	Long chain FA mitochondrial β-oxidation
Atp5f1b	ATP synthase subunit beta, mitochondrial (EC 3.6.3.14) (ATP synthase F1 subunit beta)	Negative	Oxidative phosphorylation
Atp5j2	ATP synthase subunit f, mitochondrial	Negative	Oxidative phosphorylation
Atp6v1g1	V-type proton ATPase subunit G 1 (V-ATPase subunit G 1) (V-ATPase 13 kDa subunit 1) (Vacuolar proton pump subunit G 1)	Negative	Oxidative phosphorylation
Atp6v1h	V-type proton ATPase subunit H (V-ATPase subunit H) (Vacuolar proton pump subunit H)	Negative	Oxidative phosphorylation
Cox5a	Cytochrome c oxidase subunit 5A, mitochondrial (Cytochrome c oxidase polypeptide Va)	Negative	Oxidative phosphorylation
Cyc1	Cytochrome c1, heme protein, mitochondrial (Complex III subunit 4) (Complex III subunit IV) (Cytochrome b-c1 complex subunit 4) (Ubiquinol-cytochrome-c reductase complex cytochrome c1 subunit) (Cytochrome c-1)	Negative	Oxidative phosphorylation
Ndufa2	NADH dehydrogenase [ubiquinone] 1 alpha subcomplex subunit 2 (Complex I-B8) (CI-B8) (NADH-ubiquinone oxidoreductase B8 subunit)	Negative	Oxidative phosphorylation
Ndufa3	NADH dehydrogenase [ubiquinone] 1 alpha subcomplex subunit 3 (Complex I-B9) (CI-B9) (NADH-ubiquinone oxidoreductase B9 subunit)	Negative	Oxidative phosphorylation
Ndufb2	NADH dehydrogenase [ubiquinone] 1 beta subcomplex subunit 2, mitochondrial (Complex I-AGGG) (CI-AGGG) (NADH-ubiquinone oxidoreductase AGGG subunit)	Negative	Oxidative phosphorylation
Ndufb5	NADH dehydrogenase [ubiquinone] 1 beta subcomplex subunit 5, mitochondrial (Complex I-SGDH) (CI-SGDH) (NADH-ubiquinone oxidoreductase SGDH subunit)	Negative	Oxidative phosphorylation
Ndufb6	NADH dehydrogenase [ubiquinone] 1 beta subcomplex subunit 6 (Complex I-B17) (CI-B17) (NADH-ubiquinone oxidoreductase B17 subunit)	Negative	Oxidative phosphorylation
Ndufb8	NADH dehydrogenase [ubiquinone] 1 beta subcomplex subunit 8, mitochondrial (Complex I-ASHI) (CI-ASHI) (NADH-ubiquinone oxidoreductase ASHI subunit)	Negative	Oxidative phosphorylation
Ndufc2	NADH dehydrogenase [ubiquinone] 1 subunit C2 (Complex I-B14.5b) (CI-B14.5b) (NADH-ubiquinone oxidoreductase subunit B14.5b)	Negative	Oxidative phosphorylation
Ppa2	Inorganic pyrophosphatase 2, mitochondrial (EC 3.6.1.1) (Pyrophosphate phospho-hydrolase 2) (PPase 2)	Negative	Oxidative phosphorylation
Uqcrb	Cytochrome b-c1 complex subunit 7 (Complex III subunit 7) (Complex III subunit VII) (Ubiquinol-cytochrome c reductase complex 14 kDa protein)	Negative	Oxidative phosphorylation
Uqcrh	Cytochrome b-c1 complex subunit 6, mitochondrial (Complex III subunit 6) (Complex III subunit VIII) (Cytochrome c1 non-heme 11 kDa protein) (Mitochondrial hinge protein) (Ubiquinol-cytochrome c reductase complex 11 kDa protein)	Negative	Oxidative phosphorylation
Me1	NADP-dependent malic enzyme (NADP-ME) (EC 1.1.1.40) (Malic enzyme 1)	Positive	Pyruvate synthesis and fatty acid biosynthesis
Abhd5	1-acylglycerol-3-phosphate O-acyltransferase ABHD5 (EC 2.3.1.51) (Abhydrolase domain-containing protein 5) (Lipid droplet-binding protein CGI-58) (Protein CGI-58)	Positive	TAG synthesis
Gpam	Glycerol-3-phosphate acyltransferase 1, mitochondrial (GPAT-1) (EC 2.3.1.15) (P90)	Positive	TAG synthesis

1

Table 7. Proteins involved in glucose and lipid metabolism modulated in LS-*G6pc*$^{-/-}$ mice. [a]Protein symbol retrieved from UNIPROT database. [b]Approved name of the protein. [c]Positive or Negative indicates the type of slope associated with the protein. [d]Official name of the GO biological process involving the protein. Data are listed in alphabetic order.

4.8. GSEA analysis indicates acute inflammatory and immune responses in liver from LS-*G6pc*$^{-/-}$ mice with HCA

To shed light on the molecular mechanisms underlying the development of HCA in LS-*G6pc*$^{-/-}$ livers, we performed a GSEA analysis comparing the expression profile of LS-*G6pc*$^{-/-}$ mice that developed at least one HCA with those that did not. For the analysis we used the hallmark, the C2.KEGG, and the C5.GO.BP collections of the MSigDB database.

GSEA identified 148 significantly enriched gene sets in LS-*G6pc*$^{-/-}$ mice with adenomas (Nom p-value<0.05 and FDR q-value < 0.25, data not shown). Among the gene sets identified, the most represented processes included complement and coagulation cascade, acute-phase response, acute inflammatory response, and immune response. In the complement and coagulation protein sets, we found two proteins, which play a central role in the activation of the complement system, specifically the component C3 and the component C5 (Table 8).

Protein symbol[a]	Approved name[b]	Biological process[c]
ARG1	Arginase-1	GO_IMMUNE_RESPONSE
C3	Complement component 3d (Fragment)	KEGG_COMPLEMENT_AND_COAGULATION_CASCADES
C5	Complement C5 (Hemolytic complement) [Cleaved into: Complement C5 beta chain; Complement C5 alpha chain; C5a anaphylatoxin; Complement C5 alpha'	KEGG_COMPLEMENT_AND_COAGULATION_CASCADES
CD163	Scavenger receptor cysteine-rich type 1 protein M130;Soluble CD163	GO_ACUTE_PHASE_RESPONSE
CD206	Macrophage mannose receptor 1 (MMR)	GO_INNATE_IMMUNE_RESPONSE
Mbl1	Mannose-binding protein A (MBP-A) (Mannan-binding protein) (Ra-reactive factor polysaccharide-binding component p28B) (RaRF p28B)	GO_IMMUNE_RESPONSE
MBL2	Mannose-binding protein C (MBP-C) (Mannan-binding protein) (RA-reactive factor P28A subunit) (RARF/P28A)	GO_IMMUNE_RESPONSE
STAT6	Signal transducer and transcription activator 6	GO_IMMUNE_RESPONSE

Table 8. Proteins involved in inflammatory and immune response modulated in LS-*G6pc*$^{-/-}$ mice with adenoma. [a]Protein symbol retrieved from UNIPROT database. Protein symbols are listed in alphabetic order. [b]Approved name of the protein. [c]Significantly enriched biological process assoociated with the protein by GSEA.

Among the proteins associated with the inflammatory and immune response processes, some were typical of macrophages polarized towards the alternatively activated M2 phenotype such as mannose receptor C-type 1 (CD206), a type 1 membrane lectin receptor that mediates the endocytosis of glycoproteins by macrophages; arginase 1, (ARG1), that catalyzes the hydrolysis of arginine to ornithine and urea; and the scavenger receptor MSR1, (CD163), an acute phase-regulated receptor involved in clearance and endocytosis of hemoglobin/haptoglobin complexes by macrophages. Moreover, binding lectins A (MBL1) and C (MBL2) and STAT6 were found upregulated in the liver of LS-*G6pc*$^{-/-}$ mice with HCA, suggesting accumulation of M2-polarized macrophages (Table 8) (52). Therefore, different proteins involved in the process of tissue inflammation and macrophage polarization, and thus associated with tumor progression, were identified.

These results are compatible with the pathologic environment represented by hypoxia, which was reported to affect macrophage polarization towards M2 phenotype both in rodents and in humans (58,59).

4.9. Analysis of exosomal miRNA extracted from plasma of LS-*G6pc*$^{-/-}$ mice.

Exosomes from 100 µl of plasma of 45 LS-*G6pc*$^{-/-}$ mice and relative controls were isolated. Total RNA was extracted and the presence of miRNA was evaluated by capillary electrophoresis to ensure a sufficient retrieval of material for the following analyses. The difference between a suitable and an inadequate miRNA profile is shown in figure 16A and B: a significant miRNA fraction is represented by different peaks in the region between 10-50 nucleotides, corresponding to miRNA molecules. The RNA samples with a flat profile in this region failed the quality control and were discarded from subsequent analyses.

RNA samples were reverse transcribed, pre-amplified, and used to set up a rodent microRNA array card that allowed measuring the expression of 381 targets for each sample by qRT-PCR.

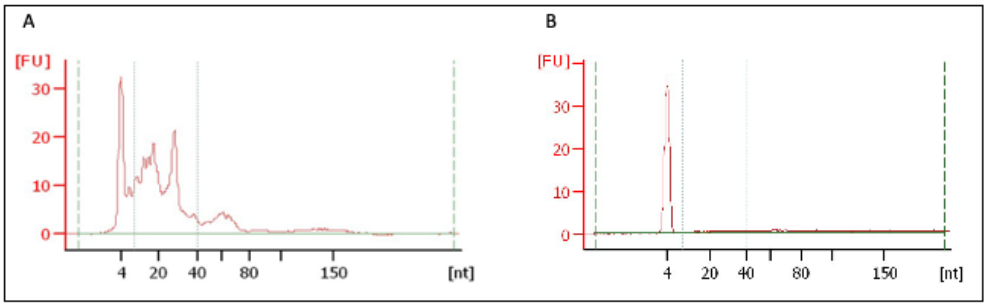

Figure 16. Small RNA profile in LS-*G6pc*$^{-/-}$ mice. The electropherogram derived from the capillary electrophoresis displays the number of nucleotides (6 to 150) on X axis and the dye fluorescence on the Y axis. Plasma was obtained from LS-G6pc$^{-/-}$ mice plasmas. The profile of the RNAs from 6 to 150 nucleotides (nt) is shown and it is measured as Fluorescence Dye Units (FU). The region between 6 to 40 nucleotides, indicated by the dashed vertical lines, includes the miRNA fraction. Here, it is shown the difference between a suitable (A) and an inadequate miRNA profile (B).

4.10. Data normalization

We performed an accurate statistical analysis of the raw qRT-PCR expression data by using ExoPipe (see methods). The raw data were normalized according to the Global Mean Method (56). The Global Mean method was effective in reducing technical variability as it is shown in Figure 17. After filtering and imputation we obtained a total number of 61 miRNA to be considered for further analysis (data not shown).

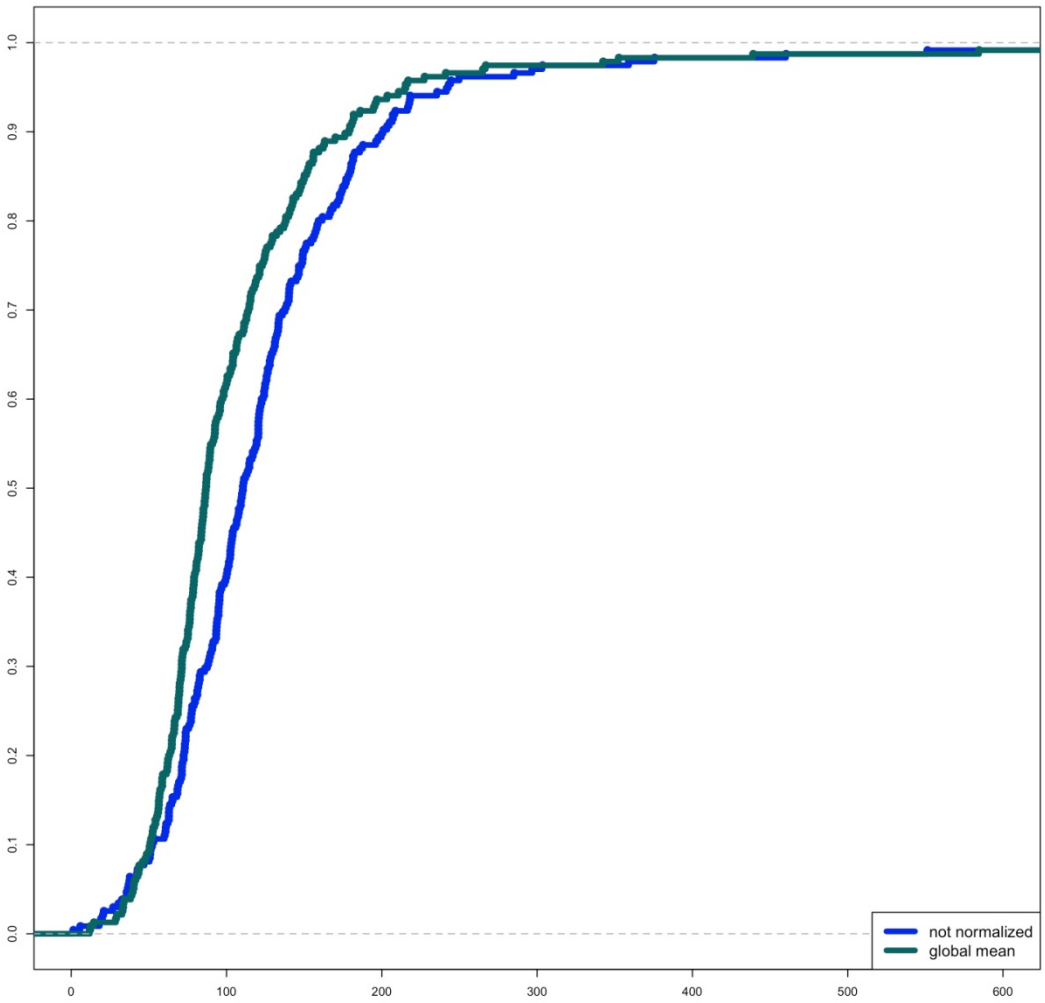

Figure 17. Cumulative distribution of miRNA coefficient of variation (CV) values. The cumulative distribution of miRNA CV values in the LS-*G6pc*$^{-/-}$ mice sample set when no normalization is applied (blue), mean expression value normalization is applied (green).

4.11. LS-*G6pc*$^{-/-}$ mice with HCA express deregulated miRNA

We compared LS-*G6pc*$^{-/-}$ mice versus WT mice and LS-*G6pc*$^{-/-}$ with HCA mice versus LS-*G6pc*$^{-/-}$ mice without HCA, to identify significantly deregulated miRNA.

Bioinformatic analysis of exo-miR identified 9 and 5 significantly deregulated miRNA in LS-*G6pc*$^{-/-}$ mice comparing with WT mice and in LS-*G6pc*$^{-/-}$ mice with adenoma compared with LS-*G6pc*$^{-/-}$ without adenoma, respectively (Table 9 and Figure 18). These miRNA were either up-regulated or down- regulated.

miRNA	LS-*G6pc*$^{-/-}$ VS WT	HCA VS no HCA
139-3p	↑	
190b	↑	
380-5p	↑	
381-5p	↑	
434-5p	↑	
24	↓	
29a	↓	
145		↓
342		↓
409	↑	
486		↓
744	↓	
192		↑
685		↓

Table 9. Differentially expressed miRNA in LS-*G6pc*$^{-/-}$ mice. The arrow's direction indicates the up- or down-regulation.

We plotted the expression of all miRNA for each mouse to visualize the deregulation of these miRNA in LS-*G6pc*$^{-/-}$ mice. Here, we selected miR-744 and miR-29a (Fig. 18A and B).

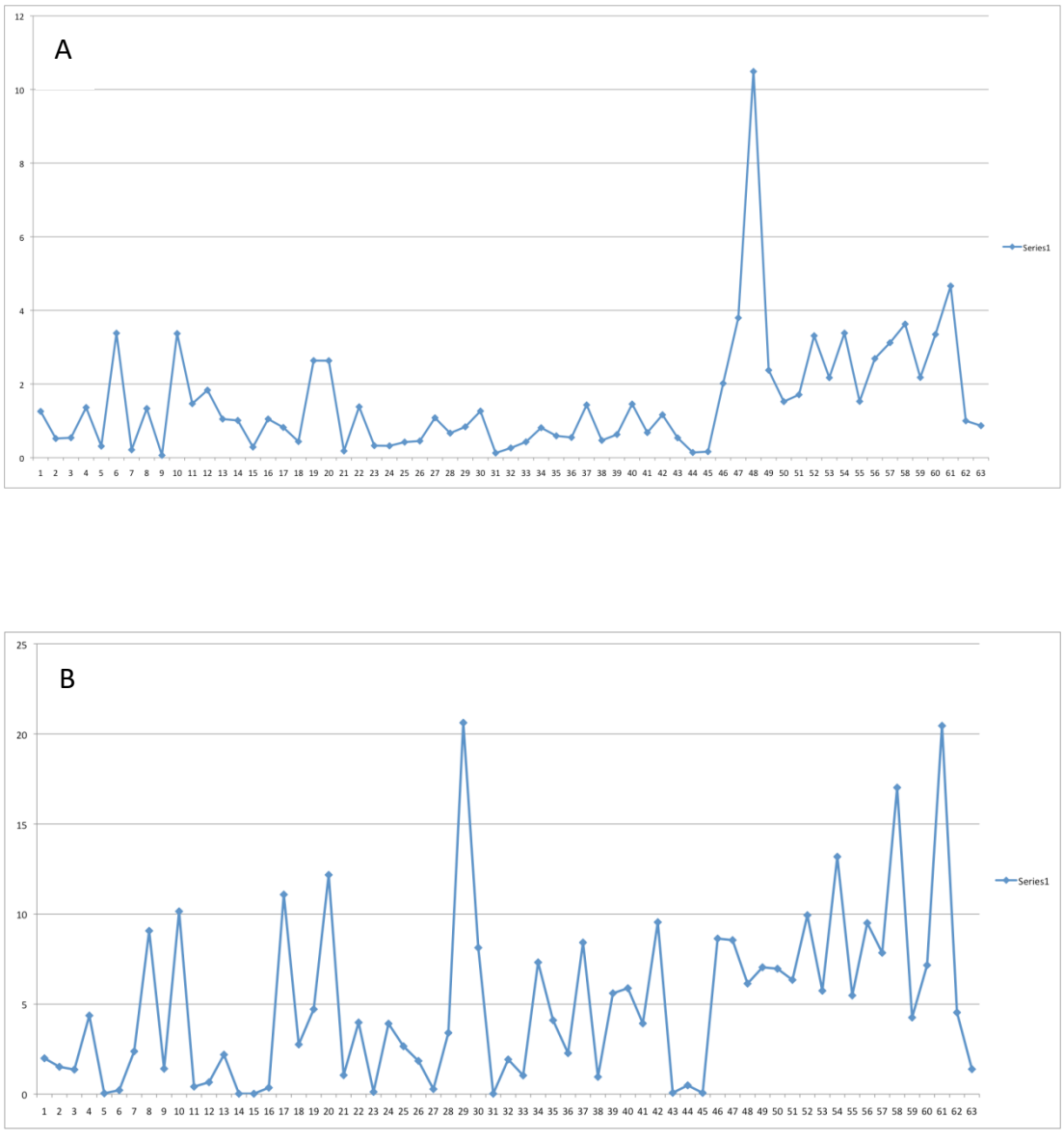

Figure 18. Scatter plot for miR-744 and miR-29a in all 63 mice.
Panels A and B show the expression of miRNA 744 and 29a. Data are relative to 45 LS-*G6pc*$^{-/-}$ and 18 WT mice. The first 45 samples refer to LS-*G6pc*$^{-/-}$. Both of these miRNA were found downregulated in LS-*G6pc*$^{-/-}$ mice.

bHCA are at a greater risk of malignant transformation into HCC. In the attempt to differentiate low-risk adenomas from high-risk adenomas, we subclassified mice in groups according with the different types of HCA they developed. We found two miRNA (miR-27a, miR-335) that seemed to be differentially expressed in mice with bHCA and/or HCC. Nevertheless, further analysis are required, since these mice show frequently adenomatosis, with the development of different types of adenomas in the same mouse, making very difficult to differentiate miRNA derived from one kind of tumor from another.

The 16 deregulated miRNA found in LS-*G6pc*$^{-/-}$ mice are linked to multiple functions and pathways. The majority of them are reported to be involved in cancer-related processes (60-64). Interestingly, some of these miRNA (miR-29a, miR-145, miR-342, miR-744, miR-335) are involved in pathways that are of potential relevance for liver disease and HCA and HCC pathophysiology. These exo-miR will be validated by qRT-PCR. Analysis of these data is still ongoing and more data will be provided in the next few months.

DISCUSSION

Several animal models of liver disease have been developed and extensively utilized in many preclinical medical research studies to investigate disease onset and progression (65-69).

Development of HCA in LS-*G6pc*$^{-/-}$ mice is the consequence of a single gene mutation that inhibits the G6Pase function and leads to liver degeneration and tumorigenesis. Thus, LS-*G6pc*$^{-/-}$ mice are of major interest because they mimic spontaneous HCA formation with aging and its evolution into HCC as in GSD1a patients.

To date there has been a lack of appropriate in vivo detection system that allows a continuous monitoring of tumor onset and progression. HCC high-risk patients are monitored through imaging surveillance, and focal nodules characterization is performed with multiphase contrast material-enhanced computed tomography and/or MRI. Because of variability in lesion interpretation, the Liver Imaging-Reporting and Data System (LI-RADS) was created with the aims of improving HCC diagnosis and therapeutic management (70).

Hepatobiliary contrast agents have significantly increased diagnostic accuracy in the detection and characterization of focal liver lesions and its role was recently recognized also in the latest version of CT/MRI LI-RADS criteria (v2017) which considers HBP as an ancillary feature in lesion characterization i.e. HPB phase hypointensity favoring malignancy in general and HBP isointensity favoring benignity (71).

We set up a protocol to assess the detection level and quantify the longitudinal evolution of liver lesions in LS-*G6pc*$^{-/-}$ mice using non-contrast T1-WI/T2-WI and non-dynamic post-contrast hepatobiliary imaging. We based our differential diagnosis on features considered ancillary by LI-RADS, especially mild to moderate T2 hyperintensity. The hepato-specific contrastographic phase allows to differentiate lesions on the basis of hepatocyte function and contrast uptake. We used Gd-BOPTA that, in the clinical practice, has high relaxivity values (72) but only 5% of biliary excretion at 1-2 hours after administration. The use of Gd-BOPTA in mice has two main advantages: hepatobiliary phase is already present about 10 minutes after contrast administration, and hepatobiliary excretion is

about 50%, because of a different pharmacokinetic profile, as previously demonstrated (73)

The detection of small HCC is challenging also in the clinical practice. In fact, the detection rate of human HCC <1 cm in diameter is only 34% (74). Our protocol allows the visualization and monitoring of small HCC/HCA nodules with a diameter of 1 mm and represents an important improvement in imaging technique of murine liver nodules compared with other study reporting some difficulty in detecting lesions ≤ 2 mm (75).

The major advantage of our protocol is the possibility to detect high-risk adenoma subtypes. In fact, by combining information of all sequences, and especially contrast enhanced T1-WI, we were able not only to detect very small size lesions but also to characterize and differentiate them into different histological HCA subtypes.

UHCA remains the less characterized adenoma subtype, with no specific genetic/pathologic abnormalities and no specific MRI pattern. In fact, UHCA showed all 4 different contrast enhancement patterns and the majority were isointense on T2-WI. During the follow up study we noticed that UHCA showing an MRI pattern typical of IHCA have a slow growth rate while UHCA with evolving features and with an MRI pattern typical of bHCA displayed a high growth rate. Bioulac-Sage and collaborators3 reported that β-catenin activation was not detected in all nodules of the same patient with adenomatosis and suggested that β-catenin mutation could occur later during adenoma carcinogenesis, promoting malignant transformation. Further studies will be required to better understand oncogenesis and identify possible differences in clinical features and pathologic and radiologic characteristics of this heterogeneous HCA subtype. In this respect, due to the rarity of UHCA, preclinical models can be useful tools to improve our knowledge in this field. Nevertheless, our results suggest that some UHCA could be considered as the precursors of bHCA at an early stage of carcinogenesis.

We show here that bHCA display MRI features distinguishable from those exhibited by IHCA or UHCA, indicating that our protocol is a reliable method to identify high risk HCA. This is an important achievement because GSD1a patients often develop multiple adenomas that may originate from independent clones and

therefore have different molecular subtypes. Because HCA is a rare disease, the information in the literature to help guide treatment is low. The possibility of characterizing the different HCA subtypes in patients with multiple adenomas is important for planning surveillance and treatment.

In conclusion, this is the first study in literature reporting the possibility to differentiate the various subtypes of hepatic adenoma using MRI imaging. In this respect, the establishment of an optimized MRI protocol to detect and analyze liver lesions in our mouse model for GSD1a opens the possibility to apply such a protocol to patients for non invasive diagnostic purposes. A very recent study utilized a similar MRI protocol to screen for HCC in patients with cirrhosis or chronic hepatitis B. Reported results indicate that MRI characteristics similar to ours are suggestive of malignant transformation (76).

Our objective was also to define a signature correlated with disease progression and tumor onset. Mass spectrometry is a very important tool for investigating protein expression and protein characteristics on a large scale (77). LC-MS-based proteomics has become a widely used technique to analyze biological samples (78,79), and its successful application has been reported in the literature for several diseases (80).

We found 1243 proteins that were modulated in livers derived from diseased animals in comparison with WT mice. In LS-*G6pc*$^{-/-}$ mice proteins involved in several metabolic processes including lactic acid production, glycolysis, pyruvate metabolism fatty acid and cholesterol biosynthesis, and response to hypoxia as well as proteins involved in inflammatory response, mitochondrial activity and immune response were modulated. The expression of many of these proteins increased or decreased over time, indicating an association between their altered expression and liver disease.

The liver is involved in metabolism and storage of nutrients in the form of glycogen and lipids and supplies energy-producing substrates to the peripheral tissues. These processes require a considerable amount of oxygen, which causes a steep oxygen gradient throughout the hepatic lobules (81). During some pathological conditions the hepatic metabolic balance can be altered resulting in disruption of hepatic oxygen homeostasis and severe liver hypoxia (81).

Hypoxia is a condition of low oxygen tension occurring in poorly or irregularly vascularized tissue areas, which has profound effects on cell growth, metabolism,

genotype selection, susceptibility to apoptosis, epithelial-to-mesenchymal transition and angiogenesis (82,83). Hypoxia is a hallmark of several human cancers and contributes to resistance to radio- and chemotherapy, tumor progression, metastatization, and poor prognosis (84-86). Although the link between hypoxia and GSD1a has not been reported, hypoxia has been implicated in the pathogenesis of a broad range of hepatic diseases including viral hepatitis, liver injury, liver fibrosis and hepatocellular carcinoma (87). We report proteomic data that suggest the presence of a hypoxic state in the livers from LS-*G6pc*$^{-/-}$ mice, irrespectively of mouse age. While overexpression of some of these proteins (ALDOA ALDOB PKLR GPI ENO1 LDHA PGK1 PFKL) is consistent with enhanced hepatic glycolytic pathway, overexpression of others (FBP1 UGP2 TPI1 PCK1) is consistent with enhanced gluconeogenesis, suggesting that both metabolic pathways are activated in LS-*G6pc*$^{-/-}$ livers. Genes belonging to the gluconeogenesis and glycolysis pathways, pH regulation, and angiogenesis are induced under hypoxic conditions. This group of genes defines a constant feature of the hypoxic status of cells of different types, origin and functional state (82). Moreover, among the proteins modulated in the livers of LS-*G6pc*$^{-/-}$, whose coding genes were part of the HALLMARK_HYPOXIA gene set (Figure 12), we observed upregulation of PDK1, a kinase that has an important role in protecting cells against apoptosis in response to hypoxia and oxidative stress, S100A4, a protein involved in the regulation of a number of cellular processes such as cell cycle progression and differentiation and whose altered expression has been implicated in tumor metastasis; LDHA which supports ATP request by glycolysis and is compatible with lactic acidemia frequently affecting GSD-1a patients. Interestingly, the production of lactate is a tumor promoting condition that support M2 polarization of macrophages (88,89) and protects tumor cells from glucose deprivation.

Thus, our findings suggest that hypoxia is a pervasive condition of LS-*G6pc*$^{-/-}$ mouse livers and highlight the possible role of hypoxia in GSD-1a, capable of affecting hepatocyte biological processes and liver microenvironment with a potential role in the progression of the disease.

LS-*G6pc*$^{-/-}$ mice also display upregulation of several enzymes involved in *de novo* biosynthesis of fatty acids (as well as their elongation and desaturation) (Table 7). This is consistent with steatosis in LS-*G6pc*$^{-/-}$ mice livers. However, livers of older

LS-*G6pc*$^{-/-}$ mice also show up-regulation of CPT1A, the enzyme that, regulating the entry of fatty acids into the mitochondria, catalyzes the rate-limiting step of mitochondrial fatty acid β-oxidation. The increase of β-oxidation could be an attempt of adaptive response to reduce the lipid overload and lipotoxicity, but the dysfunction in OXPHOS due to the downregulation of several proteins of the respiratory chain complexes and of ATP synthase, which we observed in these mice, makes this metabolism insufficient in normalizing lipid levels. In addition, the dysfunction in OXPHOS results in increased levels of mitochondrial NADH (from glycolysis and β-oxidation) that, by inducing the export of citrate and malate into the cytosol because of Krebs cycle inhibition, further promotes lipid biosynthesis as well as gluconeogenesis and cholesterol synthesis, as indicated by the upregulation by several enzymes involved in these pathways. Thus, our data from proteomic analysis sustain a metabolic reprogramming of glucose-6P leading to the accumulation of lactate, fatty acids and cholesterol, all implicated in liver damage and crucial for liver disease progression.

Interestingly, older LS-*G6pc*$^{-/-}$ mice also show upregulation of aconitase (ACO1), Aspartate aminotransferase (GOT2), alanine aminotransferase 1 (GPT), amino transferase (AT) and isocitrate dehydrogenase (IDH1), all involved in 2-oxocarboxilic acid metabolism, a process essential in hypoxic conditions and in cancer cells with mitochondrial defects (90). A summary of the metabolic pathways altered in the affected livers of aged LS-*G6pc*$^{-/-}$ mice is shown in Figure 19.

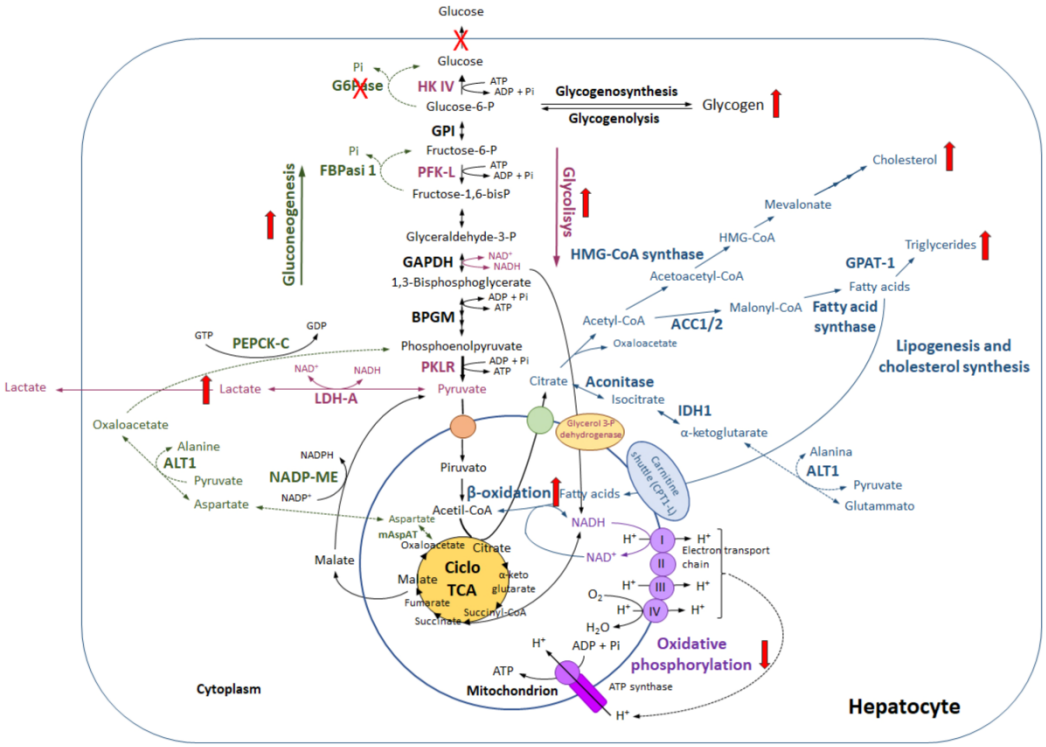

Figure 19. Diagram of the metabolism deregulation in the old mice livers. The abbreviations used for the proteins are the same as in Table 7.

Non alcoholic fatty liver disease, NAFLD, is a liver disorder characterized by the presence of steatosis in more than 5% of hepatocytes and is not correlated with alcohol consumption (91). NAFLD has frequently been associated with obesity, type 2 diabetes mellitus, hyperlipidemia, and insulin resistance and, for this reason; it is considered the hepatic manifestation of the metabolic syndrome (92). Moreover, patients with NAFLD are at an increased risk of developing HCC (93). The molecular mechanisms that underlie the pathophysiological changes of hepatic lipid metabolism in NAFLD include inflammation, drug metabolism, synthesis of endogenous fatty acids, lipotoxicity, and PPARs activation (94). Moreover, the Cytochrome P450 epoxygenase pathway has been indicated as another important regulator of the hepatic inflammatory response in mice with fatty liver disease (95). During NAFLD, several metabolic adaptations are set up by mitochondria in order to restrain fat accumulation. Some of these mechanisms, such as mitochondrial fatty acid oxidation, may aggravate oxidative stress and

impair energy output resulting in severe mitochondrial dysfunction (96). Finally, macrophage polarization and inflammatory signals appear to be central for the pathogenesis and progression of NAFLD (97). With this analysis, we have identified a set of significantly altered proteins in LS-*G6pc*$^{-/-}$, respect to wild type mice, that are involved in NAFLD, i.e. innate immune response, inflammatory response and mitochondrion dysfunction, suggesting that LS-*G6pc*$^{-/-}$ mice are affected by NAFLD.

We performed a proteomic analysis of liver samples from LS-*G6pc*$^{-/-}$ mice that had developed HCA in comparison with liver samples from mice that had not. Among proteins identified in LS-*G6pc*$^{-/-}$ mice developing adenomas, we identified two important complement components, the component C3, which modulates inflammation, and the component C5, which is part of the innate immune system and plays an important role in inflammation, host homeostasis and host defense against pathogens. These proteins play a key role in the regulation of inflammatory cells accumulation in the tissues. In particular, C5 seems to be important for the recruitment of myeloid-derived suppressor cells, which promote immunosuppression that is linked to tumor growth (98,99). Macrophages represent a major component of the leukocyte infiltrate at sites of inflammation infection, tissue damage and tumor growth and can differentiate into a spectrum of phenotypic states in response to diverse environmental signals (98).

The classically activated (type 1 proinflammatory or M1) macrophages display proinflammatory and effector properties and mediate antimicrobial defense, tissue destruction, and antitumor resistance (98,99). Conversely, the alternatively activated (type 2 anti-inflammatory or M2) macrophages exhibit tissue remodeling and repair functions, promote wound healing, angiogenesis, and resistance to parasites (98,99), they accumulate in most human cancers (tumor associated macrophages, TAMs), supporting tumor progression, metastatic dissemination and cancer immune evasion (100,101).

Macrophages are a key component of the homeostatic functions of the liver. In response to damaged liver tissue, macrophages undergo polarization into M1 or M2 activation states, mirroring in vitro polarized mononuclear phagocytes (98).

Interestingly, we found upregulation of several markers of macrophage polarization towards the M2 phenotype in the liver of mice with HCA, including the mannose receptor C-type 1, arginase 1, the scavenger receptor CD163, and

STAT6, suggesting the accumulation in the liver of M2-polarized macrophages. We also found that the expression of these markers in the livers of LS-*G6pc*$^{-/-}$ mice is modulated in an age dependent manner (data not shown). Therefore, M2 type macrophages are present in these livers and their accumulation may correlate with tumor onset and progression. Inflamed livers express high levels of lectin receptors, such as CLEC4D and CLEC4E, which respond to the microenvironment by promoting the innate response (52). In this respect, mannose binding lectins A and C are upregulated in LS-*G6pc*$^{-/-}$ mice livers.

All these results are compatible with the hypoxic pathologic environment of LS-*G6pc*$^{-/-}$ mice livers, The role of hypoxia in macrophage polarization is in fact beginning to emerge 102,103) and hypoxia is known to upregulate M2 markers both in rodent and in human macrophages (58,59). In addition, lactic acid produced in LS-*G6pc*$^{-/-}$ mice livers as a by-product of aerobic or anaerobic glycolysis, typically indicative of hypoxia, may be important for inducing the accumulation of M2-polarized macrophages. Colegio and coworkers (104) demonstrated that lactic acid, produced by tumor cells, has a critical function in inducing M2-like polarization of tumor-associated macrophages and macrophage expression of arginase 1, which has an important role in tumor growth. Cells of the monocyte-macrophage lineage are crucial drivers of tumor-promoting inflammation and play a key role in cancer, contributing to tumor progression (105). Therefore, the hypoxic state of LS-*G6pc*$^{-/-}$ livers combined with promotion of macrophage polarization towards M2 phenotype may represent the environmental condition for hepatic tumor development and progression and can provide tools to tailor cytoreductive therapies and immunotherapy.

These results identify a metabolic reprogramming of glucose-6-P and a pathologic environment in the liver of GSD-1a mice compatible with tumor development and progression.

We also evaluated whether miRNA may represent potential biomarkers of tumor onset and progression in GSD1a. We studied exosomes derived from peripheral blood of LS-*G6pc*$^{-/-}$ mice, comparing the expression profile of exo-miR in mice with different clinical characteristics to determine whether miRNA differential expression can be indicative of tumor onset and progression. An advantage of using the LS-*G6pc*$^{-/-}$ mice was the possibility to perform a preliminary analysis in a homogenous model, with a common genetic background and uniform disease

progression. This initial approach allowed us to identify and select a restricted number of miRNA that are dysregulated in GSD1a. These miRNA were subjected to a bioinformatic analysis to gather information on their possible role in GSD1a pathophysiology and HCA development.

The miRNA we found to be dysregulated in GSD1a mice with tumor were potentially relevant for the disease pathophysiology according to the bioinformatic and literature analysis (106-110). Furthermore they were measurable in samples, like plasma, that can be readily available in patients and require minimally invasive procedures. Among the dysregulated miRNA, miR-29a, miR-145, miR-342, miR-744 and miR-335were particularly attractive, because they had already been proposed as a biomarker for liver diseases and liver tumorigenesis (60-64), and may allow for the identification of a specific "signature" of HCA onset, and of disease progression, outcome, or response to therapies. In summary, our results demonstrate that the blood of LS-*G6pc*$^{-/-}$ mice contains tumor-specific exosomes and that exo-miR can efficiently be isolated from plasma specimens and may be used as prognostic/diagnostic biomarkers.

The exosomal miRNA signatures we have derived represent the liver specific contribution to the exosomal miRNA profile of HCA development. Moreover, further analysis may allow a correlation between miRNA profile and bHCA, of particular prognostic relevance for the development of HCC.

The mouse model utilized has allowed the clear definition of the liver contribution to the exosomal miRNA profile because it is the only organ affected by the deletion of the G6pPase-α. Our model has been an essential tool to study the role of exosomal miRNA in the onset of HCA and HCC. miRNA that we have identified can be used as biomarkers for the onset and the malignant transformation of hepatic tumors. Our results could be useful for therapeutic strategies against liver degeneration that leads to HCA and HCC, and for prevention and/or cure of HCA and HCC in other pathological conditions.

The ongoing and future studies are focused on:

Correlate miRNA expression with HCA progression over time.

We will evaluate exo-miR profile during the evolution of liver lesions detected and quantified with the MRI protocol we developed.

Mice will be periodically analyzed for the presence of HCA, starting at the age of 10-11 months, by MRI.

This analysis will determine the presence or absence of HCA, their subdivision in IHCA, bHCA and UHCA and/or HCC to be correlated with the exo-miR profile that will be determined from plasma samples collected at each MRI analysis. Mice will be sacrificed after the last MRI session at the age of 16-17 month, and HCA classification will be confirmed by immunohistochemistry.

Correlate miRNA expression of LS mice with miRNA expression in GSD1a patients.

We have established a collaboration with Dr. M. Di Rocco (Unit of Rare Diseases, Department of Pediatrics, G. Gaslini Institute, Genova), Dr. Daniela Melis (Department of Translational Medical Sciences, Section of Pediatrics, Federico II University, Napoli), Prof. Enrica Riva (Department of Pediatrics, San Paolo Hospital, University of Milano), Dr. Annalisa Sechi (Regional Coordinator Center for Rare Diseases, University Hospital "Santa Maria della Misericordia, Udine), and Dr. David Weinstein (Connecticut Children's Hospital, Farmington, Ct, USA) who have recruited the GSD1a patients to be included in this project.

Patients between one and 45 years of age, undergoing periodic evaluation, have been included in the study. Age matched healthy donors have been enrolled as control. Presently, we have already extracted exo-MiR from the plasma of 80 patients. This cohort represents a substantial number of cases sufficient for statistical evaluation. The low number of patients at risk of HCC may be an obstacle for statistical evaluation. Should this be the case, we will rely on the mouse model data to map the exosomal miRNA profile for a correlative support of the findings. miRNA bioinformatic analysis is already ongoing, and as a result of this analysis, we will identify the human miRNA signatures characterizing the presence of adenomas in GSD1a patients. These miRNA can allow an early

prediction of the adenoma development, and could be used to develop protocols for the therapeutic targeting of miRNA.

In fact, pathological expression of miRNA can be controlled by a new generation of drugs that, by antagonizing or restoring miRNA function in the target cell, attempt to normalize the homeostasis of the tissue. miRNA-targeting therapies are an area of strong interest and many such compounds are in preclinical and clinical development for a variety of diseases. miRNA mimic molecules and antisense inhibitors are in phase I or preclinical studies for treatment of cancer, including hepatocellular carcinoma and glioblastoma, and other human diseases such as heart failure and insulin resistance (111).

We hope that our findings may be translated to the human setting and therefore may constitute the basis for the development of an appropriate screening and therapeutic protocol for patients.

REFERENCES

1. Stoot JH, Coelen RJ, De Jong MC, Dejong CH. HPB (Oxford) 2010; 12:509-22.

2. Dokmak S, Paradis V, Vilgrain V, et al. Gastroenterology 2009;137:1698–1705.

3. Bioulac-Sage P, Rebouissou S, Thomas C, et al. Hepatology 2007;46:740–748.

4. Bioulac-Sage P, Laumonier H, Couchy G, et al. Hepatology 2009;50:481–489.

5. Zucman-Rossi J, Jeannot E, Nhieu JT, et al. Hepatology 2006;43:515–524.

6. Bluteau O, Jeannot E, Bioulac-Sage P, et al. Nat Genet 2002;32:312–315.

7. Rebouissou S, Bioulac-Sage P, Zucman-Rossi J. J Hepatol 2008;48:163–170.

8. Rebouissou S, Amessou M, Couchy G, et al. Nature 2009;57:200–204.

9. Bioulac-Sage P, Sempoux C, Possenti L et al. Int J Hepatol 2013; 2013:253261

10. Farges O, Ferreira N, Dokmak S, et al. Gut 2011; 60:85-9

11. Chou JY, Matern D, Mansfield BC, et al. Curr Mol Med 2002; 2:121-43

12. Lei KJ, Shelly LL, Pan CJ, et al. Science 1993; 262:580-3

13. Nordlie, RC and Sukalski, KA (1985) in The Enzymes of Biological Membranes (Martonosi, AN, ed.) Plenum Press, New York, 2nd Ed., pp. 349- 398.

14. Greene, HL, Slonim, AE, O'Neil, JA et al. N Engl J Med 1976; 294, 423-425.

15. Chen, YT, Cornblath, M and Sidbury, JB. N Engl J Med 1984;310, 171-175.

16. Franco LM, Krishnamurthy V, Bali D et al. J Inherit Metab Dis 2005; 28:153-62

17. Labrune P, Trioche P, Duvaltier I, et al. J Pediatr Gastroenterol Nutr 1997; 24:276-9

18. Reddy SK, Kishnani PS, Sullivan JA, et al. J Hepatol 2007; 47:658-63

19. Calderaro J, Labrune P, Morcrette G, et al. J Hepatol 2013;58:350-7.

20. Chou JY, Jun HS, Mansfield BC. Nat Rev Endocrinol 2010; 6:676-88

21. Lei KJ, Chen H, Pan CJ, et al. Nat Genet 1996;13, 203–209

22. Resaz R, Vanni C, Segalerba D, et al. Dis Model Mech 2014;7:1083-91.

23. Poe R., Snover D. C. Am J Surg Pathol 1988;12, 477–483

24. Oliva MR, Saini S. Cancer Imaging 2004;4 Spec No A:S42-S46.

25. Laumonier H, Bioulac-Sage P, Laurent C, et al. Hepatology 2008;48:808-18.

26. van Aalten SM, Thomeer MG, Terkivatan T, et al. Radiology 2011;261:172-81.

27. Yoneda N, Matsui O, Kitao A, et al. Jpn J Radiol 2012;30:777-82.

28. Lundberg E, Fagerberg L, Klevebring D, et al. Mol Syst Biol 2010;6:450.

29. Sharma K, Schmitt S, Bergner CG, et al. Nat Neurosci 2015;18:1819-31.

30. Jiang X, Zeng T, Zhang S, et al. PLoS One 2013;8:e80698.

31. El-Aneed A, Banoub J. Anticancer Res 2006;26:3293-300.

32. Parent R, Beretta L. J Hepatol 2005;43:177-83.

33. Ratajczak J, Wysoczynski M, Hayek F, et al. Leukemia 2006; 20:1487-95

34. Mack M, Kleinschmidt A, Bruhl H, et al. Nat Med 2000; 6:769-75

35. Al-Nedawi K, Meehan B, Micallef J, et al. Nat Cell Biol 2008; 10:619-24 4. 9

36. Valadi H, Ekstrom K, Bossios A, et al. Nat Cell Biol 2007; 9:654-9

37. Baj-Krzyworzeka M, Szatanek R, Weglarczyk K, et al. Cancer Immunol Immunother 2006; 55:808-18

38. Janowska-Wieczorek A, Wysoczynski M, Kijowski J, et al. Int J Cancer 2005; 113:752-60

39. Millimaggi D, Mari M, D'Ascenzo S, et al. Neoplasia 2007; 9:349-57

40. Tickner JA, Urquhart AJ, Stephenson SA, et al. Front Oncol 2014; 4:127

41. Hu G, Drescher KM, Chen XM. Front Genet 2012; 3:56

42. Ngu S, Lebron-Zapata L, Pomeranz C, et al. Abdom Radiol (NY). 2016;41:50-5.

43. Cox J, Mann M. Nat Biotechnol 2008;26:1367-72.

44. Cox J, Michalski A, Mann M. J Am Soc Mass Spectrom 2011;22:1373-80.

45. Cox J, Neuhauser N, Michalski A, et al. J Proteome Res 2011;10:1794-805.

46. Cox J, Hein MY, Luber CA, et al. Mol Cell Proteomics 2014;13:2513-26.

47. Vizcaino JA, Csordas A, del-Toro N, et al. Nucleic Acids Res. 2016;44:D447-D456.

48. Metsalu T, Vilo J. ClustVis: Nucleic Acids Res. 2015;43:W566-W570.

49. Tusher VG, Tibshirani R, Chu G. Proc Natl Acad Sci U S A. 2001;98:5116-21.

50. Szklarczyk D, Franceschini A, Wyder S, et al. Nucleic Acids Res. 2015;43:D447-D452.

51. Subramanian A, Tamayo P, Mootha VK, et al. Proc Natl Acad Sci U S A. 2005;102:15545-50.

52. Liberzon A, Subramanian A, Pinchback R, et al. Bioinformatics. 2011;27:1739-40.

53. Dvinge H, Bertone P. Bioinformatics 2009;25(24), 3325.

54. Friedman J, Hastie T, Tibshirani R. Journal of Statistical Software 2010;33(1), 1-22.

55. Mestdagh P, Vandesompele J. Nature Methods 2014;11, 809–815

56. Mestdagh P, Van Vlierberghe P, De Weer A, et al. Genome Biol 2009;10, R64.

57. Hong, F, Breitling, R, McEntee, WC et al. Bioinformatics 2006;22, 2825-2827

58. Murray PJ, Wynn TA. Nat Rev Immunol. 2011;11:723-37.

59. Leblond MM, Gerault AN, Corroyer-Dulmont A, et al. Oncoimmunology. 2016;5:e1056442.

60. Zhang Y, Yang L, Wang S, et al. Cancer Biomark. 2018;22(1):151-159.

61. Wang W, Xiao X, Chen X et al. Int J Cancer. 2018 Jan 15;142(2):308-321.

62. Liu W, Kang L, Han J, et al. Onco Targets Ther 2018 Mar 23;11:1643-1653.

63. Tan YL, Bai ZG, Zou WL, et al. Clin Res Hepatol Gastroenterol. 2015

64. Wang F, Li L, Piontek K, et al. Hepatology. 2018 Mar;67(3):940-954.

65. Fausto N, Campbell JS. Semin. Liver Dis. 2010;30:87-98.

66. Gabele E, Dostert K, Dorn C et al. Alcohol Clin. Exp. Res. 2011;35:1361-1367.

67. Jacobs A, Warda AS, Verbeek J, et al. Curr. Protoc. Mouse Biol. 2016;6:185-200.

68. He L, Tian DA, Li PY, et al. Oncotarget 2015;6:23306-22.

69. Yan AW, Fouts DE, Brandl J, et al. Hepatology.2011;53:96-105.

70. Purysko AS, Remer EM, Coppa CP, et al. Radiographics. 2012;32:1977-1995.

71. Elsayes KM, Hooker JC, Agrons MM, et al. Radiographics. 2017;37:1994-2017.

72. Shellock FG, Parker JR, Pirovano G, et al. J. Magn. Reson. Imaging. 2006;24:1378-85.

73. Lorusso V, Arbughi T, Tirone P, et al. J. Comput. Assist. Tomogr. 1999;23 Suppl 1:S181-S194.

74. Lauenstein TC, Salman K, Morreira R, et al. Am. J. Roentgenol. 2007;189:663-70.

75. Freimuth J, Gassler N, Moro N, et al. Mol. Cancer. 2010;9:94.

76. Tillman BG, Gorman JD, Hru JM et al. Clin. Radiol. 2018;73 485-493.

77. Yates JR, Ruse CI, Nakorchevsky A. Annu Rev Biomed Eng. 2009;11:49-79.

78. Aebersold R, Mann M. Nature. 2003;422:198-207.

79. Han X, Aslanian A, Yates JR, III. Curr Opin Chem Biol. 2008;12:483-90.

80. Jimenez CR, Zhang H, Kinsinger CR, Nice EC. Clin Proteomics. 2018;15:4.

81. Suzuki T, Shinjo S, Arai T, et al. World J Gastroenterol. 2014;20:15087-97.

82. Semenza GL. N Engl J Med. 2011;365:537-47.

83. Bosco MC, Varesio L. in Melillo G editor, editor. Hypoxia and cancer. Biological implications and therapeutic opportunities. Humana Press; 2013. p. 91-119.

84. Pahlman S, Mohlin S. Cell Tissue Res. 2018;372:269-75.

85. Harris BH, Barberis A, West CM, et al. Clin Oncol (R Coll Radiol). 2015;27:547-60.

86. Chen C, Lou T. Oncotarget. 2017;8:46691-703.

87. Nath B, Szabo G. Hepatology. 2012;55:622-33.

88. Hu X, Chao M, Wu H. Signal Transduct Target Ther. 2017;2:16047.

89. San-Millan I, Brooks GA. Carcinogenesis. 2017;38:119-33.

90. Castelli G, Pelosi E, Testa U. Cancers (Basel). 2017;9.

91. Cobbina E, Akhlaghi F. Drug Metab Rev. 2017;49:197-211.

92. Naik A, Belic A, Zanger UM, et al. Front Genet. 2013;4:2.

93. Michelotti GA, Machado MV, Diehl AM. Nat Rev Gastroenterol Hepatol. 2013;10:656-65.

94. Berlanga A, Guiu-Jurado E, Porras JA, et al. Clin Exp Gastroenterol. 2014;7:221-39.

95. Schuck RN, Zha W, Edin ML, et al. PLoS One. 2014;9:e110162.

96. Begriche K, Massart J, Robin MA, et al. Hepatology. 2013;58:1497-507.

97. Alisi A, Carpino G, Oliveira FL, et al. Mediators Inflamm. 2017;2017:8162421.

98. Sica A, Invernizzi P, Mantovani A. Hepatology. 2014;59:2034-42.

99. Mosser DM, Edwards JP. Nat Rev Immunol. 2008;8:958-69.

100. Biswas SK, Allavena P, Mantovani A. Semin Immunopathol. 2013;35:585-600.

101. Qian BZ, Pollard JW. Cell. 2010;141:39-51.

102. Escribese MM, Casas M, Corbi AL. Immunobiology. 2012;217:1233-40.

103. Raggi F, Pelassa S, Pierobon D, et al. Front Immunol. 2017;8:1097.

104. Colegio OR, Chu NQ, Szabo AL, et al. Nature. 2014;513:559-63.

105. Mantovani A, Marchesi F, Malesci A, et al. Nat Rev Clin Onco.l 2017;14:399-416.

106. Zhu Y, Zhou C, He Q. J Int Med Res. 2018 Nov 5:300060518802727.

107. Li W, Yu ZX, Ma BF. Eur Rev Med Pharmacol Sci 2018 Sep;22(17):5490-5498.

108. Chen Y, Zhang F, Zhao Y et al. Onco Targets Ther. 2018 Jun 1;11:3281-3292.

109. Zhang CS, Lin Y, Sun FB, et al. Eur Rev Med Pharmacol Sci. 2019 Jan;23(1):146-154.

110. Chen J, Yu Y, Chen X, et al. Cell Prolif. 2018 Dec;51(6):e12510.

111. Li Z, Rana TM. Therapeutic targeting of microRNAs: current status and future challenges. Nat Rev Drug Discov 2014 Aug;13(8):622-638.

PUBLICATIONS

"Characterization of high- and low- risk hepatocellular adenomas by resonance imaging in an animal model of glycogen storage disease type 1a."
Roberta Resaz, Francesca Rosa, Federica Grillo, Luca Basso, Daniela Segalerba, Andrea Puglisi, Maria Carla Bosco, Luca Mastracci, Carlo E. Neumaier, Luigi Varesio and Alessandra Eva.
Under revision.

"Development and characterization of an inducible mouse model for glycogen storage disease type 1b."
Federica Raggi*, Anna Livia Pissavino*, **Roberta Resaz***, Daniela Segalerba, Andrea Puglisi, Francesca Antonini, Genny Del Zotto, Alessandra Gamberucci, Paola Marcolongo, Maria Carla Bosco, Federica Grillo, Luca Mastracci and Alessandra Eva.
J Inherit Metab Dis. 2018 Nov;41(6):1015-1025.

"A proteomic analysis of GSD1a in mouse livers: evidence for metabolic reprogramming, inflammation and macrophage polarization"
Davide Cangelosi*, **Roberta Resaz***, Andrea Petretto, Daniela Segalerba, Luca Mastracci, Federica Grillo, Maria Carla Bosco, Luigi Varesio, Antonio Sica, Irma Colombo, Alessandra Eva.
Under revision.

* These authors contributed equally to this work.